

# Electrically Small Dipole Antenna Probe for Quasi-static Electric Field Measurements

by

Adnan Zolj  
B.S. Electrical Science and Engineering  
Massachusetts Institute of Technology, 2010

SUBMITTED TO THE DEPARTMENT OF ELECTRICAL AND COMPUTER ENGINEERING  
IN PARTIAL FULFILLMENT OF THE REQUIREMENTS FOR THE DEGREE OF

MASTER OF SCIENCE  
IN ELECTRICAL AND COMPUTER ENGINEERING AT THE  
WORCESTER POLYTECHNIC INSTITUTE

MARCH 2018

© 2018 Adnan Zolj. All rights reserved.

The author hereby grants WPI permission to reproduce  
And to distribute publicly paper and electronic  
Copies of this thesis document in whole or in part  
In any medium now known or hereafter created.

Signature of Author: \_\_\_\_\_  
Department of Electrical and Computer Engineering  
March 23, 2018

Approved By: \_\_\_\_\_  
Dr. Sergey Makarov  
Thesis Supervisor

Approved By: \_\_\_\_\_  
Dr. Aapo Nummenmaa  
Thesis Committee Member

Approved By: \_\_\_\_\_  
Dr. Greg Noetscher  
Thesis Committee Member

Approved By: \_\_\_\_\_  
Dr. Reinhold Ludwig  
Thesis Committee Member

Accepted By: \_\_\_\_\_  
Dr. John A. McNeill  
Department Head

# Electrically Small Dipole Antenna Probe for Quasi-static Electric Field Measurements

by

Adnan Zolj

Submitted to the Department of Electrical and Computer Engineering  
on March 23, 2018 in Partial Fulfillment of the  
Requirements for the Degree of Master of Science in  
Electrical and Computer Engineering

## ABSTRACT

The thesis designs, constructs, and tests an electrically small dipole antenna probe for the measurement of electric field distributions induced by a transcranial magnetic stimulation (TMS) coil. Its unique features include high spatial resolution, large frequency band from 100 Hz to 300 kHz, efficient feedline isolation via a printed Dyson balun, and accurate mitigation of noise. Prior work in this area is thoroughly reviewed. The proposed probe design is realized in hardware; implementation details and design tradeoffs are described. Test data is presented for the measurement of a CW capacitor electric field, demonstrating the probe's ability to properly measure conservative electric fields caused by a charge distribution. Test data is also presented for the measurement of a CW solenoidal electric field, demonstrating the probe's ability to measure non-conservative solenoidal electric fields caused by Faraday's law of induction. Those are the primary fields for the transcranial magnetic stimulation. Advantages and disadvantages of this probing system versus those of prior works are discussed. Further refinement steps necessary for the development of this probe as a valuable TMS instrument are discussed.

Thesis Supervisor: Sergey Makarov

Title: Professor of Electrical and Computer Engineering

## **Preface with Acknowledgements**

I would like to thank Vicor Corporation for their generous financial support of my master's studies for which this thesis is but a part. I would like to thank Dr. Sergey Makarov, Dr. Aapo Nummenmaa and Dr. Lucia Navarro de Lara for their mentorship on this thesis. I would like to thank Mr. Franco Baudino for his assistance in the initial prototyping and initial discussions of this thesis.

# TABLE OF CONTENTS

---

List of Figures .....	v
List of Tables .....	vii
1 Introduction .....	1
1.1 Prior Work on Electric Field Probes for TMS Characterization .....	1
1.1.1 Bioelectrode-based Electric Field Probes.....	2
1.1.2 $\partial B/\partial t$ probes using a small loop.....	4
1.1.3 $\partial B/\partial t$ probes using a long rectangular loop.....	4
1.1.4 $\partial B/\partial t$ probes using a triangular loop .....	4
1.2 Other Prior Work on Probes for EM Field Measurements .....	5
1.2.1 Small Dipole with Capacitive Load .....	5
1.2.2 Small Dipole with Diode/Thermocouple Loads.....	6
1.2.3 Electro-optic Probes.....	6
1.3 Contribution of this Work .....	7
2 Electrical Design and Implementation .....	9
2.1 Dipole and Balun Hardware .....	9
2.2 Instrumentation Hardware .....	11
2.3 Design Process and Tradeoffs .....	12
2.4 Final Design Parameters .....	14
3 Experimental Procedures and Setup.....	16
3.1 Frequency Response .....	16
3.1.1 Differential-mode Gain .....	16
3.1.2 Common-mode Gain.....	16
3.2 Transient Response.....	16
3.3 Quasistatic Electric Field of Parallel Plate Capacitor.....	17
3.4 Quasistatic Electric Field of Solenoid .....	17
4 Experimental Results and Discussion.....	19
4.1 Frequency Response .....	19
4.1.1 Differential-mode Gain .....	19
4.1.2 Common-mode Gain.....	20
4.2 Transient Response.....	20
4.3 Quasistatic Electric Field of Parallel Plate Capacitor.....	21

4.4	Quasistatic Electric Field of Solenoid .....	23
5	Conclusion and Future Work .....	27
6	Bibliography .....	29
7	Appendix A: Ancillary Circuitry on Instrumentation PCB.....	33
8	Appendix B: Soft-switched MOSFET-based Stimulator.....	36

# LIST OF FIGURES

---

Figure 1: The following is a caricature of the loaded probe concept as proposed by Swiontek [8]. The bioelectrode surfaces normal to the current density being measured are processed to have a very low charge transfer resistance,  $R_{CT}$ . As such current readily enters the loaded probe forming a current divider with the medium. The load resistor is chosen to match the current density at the low  $R_{CT}$  surfaces of the probe with that of the medium. .... 3

Figure 2: a) – Zoom-in of the 5mm printed dipole; b) – the dipole, balun and instrumentation assembled together; c) – a simplified schematic for the complete electric field probe; biasing and other ancillary circuitry are omitted. .... 9

Figure 3: Stackup for PCB of dipole and balun. Copper layers are 1 oz. thick (1.35mils). Prepreg thickness between layers 1-2 and layers 3-4 is around 9.5mils. Thickness of center core material between layers 2-3 is about 39mils. .... 10

Figure 4: Top view of PCB for dipole and balun. Dipole and feedlines are shown on layer 2. Layers 1,3, 4 are the shield of the balun. The layers are stitched together with the vias denoted as green dots..... 10

Figure 5: Photograph showing the rework needed to eliminate the loop made by the SMA connector assembly required by the partitioning of the design into two PCBs. The feedlines are cut on the top layer before they reach the pads for the SMA center conductors on both the dipole/balun PCB and the instrumentation PCB. The feedlines are routed through air using a differential pair made using AWG32 insulated wire. .... 11

Figure 6: PCB artwork for the 2-layer, 0.062" FR4-based PCB for the instrumentation. The bottom layer (blue) is mainly used as ground plane. The top layer (red) is used for routing. The split between the floating and grounded sides of the optical isolation boundary is illustrated using the diagonal strip pattern in the silk-screening. .... 12

Figure 7. a) – Simplified INA half-circuit noise model; b) – computed signal-to-noise ratio following Eq. (1); note that  $i_n$  is set to 0 for these calculations. .... 13

Figure 8: This is a repeat of Figure 2c) to improve the readability of this section ..... 15

Figure 9: Parallel plate capacitor setup for parallel capacitor experiments..... 17

Figure 10: Shield is placed between length of coil and dipole oriented along the circulating magnetic vector potential of the coil..... 18

Figure 11: The differential mode conversion factor is normalized to the data point at 3kHz. The conversion factor at 3kHz is 0.227V on the output for 1V/cm of input electric field strength..... 19

Figure 12.. The common-mode gain is due to the parasitic capacitance bridging the isolation barrier of the HCNR201..... 20

Figure 13. Transient response of the probe. CH1 (blue) is voltage of the driven plate of the parallel plate capacitor. CH2 (red) is the output voltage of the electric field probe. a) –AC-coupled probe output response to a 100 Hz square wave; b) – response to a 10 kHz square wave; c) – response to a 100 kHz square wave with an artifact; d) –the same result as in c) but after shorting the isolation barrier..... 21

Figure 14. Vector field plot of electric field. Only x-hat components of the E-field were measured in the region from  $x=0$  to  $x=4$  and  $y=-4$  to  $y=4$ ..... 22

Figure 15: Streamlines of the E-field vector field shown in Figure 14. .... 22

Figure 16. Dominant electric-field component inside and outside the parallel-plate capacitor setup described in section 4.3. The dotted lines represent the capacitor plates. The capacitors were driven by a

differential voltage amplitude of 7.6V, corresponding to an expected field strength of 1.84V/cm between the plates. ....	23
Figure 17: The coil setup of section 3.4 was altered to align the dipole wings along the length of the coil where there is naturally no $-\partial A/\partial t$ . The left waveform in Figure 17 measures the probe output voltage when there is no shield between the dipole and the coil. The right waveform measures the probe output voltage when the shield is inserted. ....	24
Figure 18: Initial data reduction comparing measured data to expected data for the solenoidal field tests .....	24
Figure 19: Illustration showing parasitic dB/dt loop made by SMA connector bridge.....	25
Figure 20: Expected Probe output when only the contribution from the dB/dt loop is include.....	25
Figure 21. The measured dA/dt versus the expected dA/dt as evaluated by the expression in [39] .....	26
Figure 22: Measured induced electric field waveform at $x=4.524\text{cm}$ ; the SNR at these measurement amplitudes was improved by averaging the waveform 64 times resulting in the waveform shown. CH1 (blue) is the coil current measured with a separate current probe in series with the coil, and CH2 (red) is the output voltage of the electric-field probe. The excitation frequency is 3.846kHz.....	26
Figure 23. Block diagram showing battery power and push-button state machine .....	33
Figure 24. Placement of blocks shown in Fig. 23. ....	34
Figure 25. Simple FSM for high-pass filter (HPF) bypass and ON/RESET control.....	34
Figure 26. This plot shows the measured differential mode gain response with the high-pass filter enabled. The high-pass filter was implemented as a 4 <sup>th</sup> order Bessel filter with corner frequency at 360Hz, providing 50dB of attenuation at 60Hz. The data was normalized to the conversion gain at 3kHz, which measured to be 0.227V of output voltage for 1V/cm of incident electric field. The inclusion of this filter was intended as a test-mode. ....	35
Figure 27. Schematic for a bi-stable current pulse generator for induced E-field measurements with a solenoid. Decoupling/bypass capacitors and unused circuits (in multi-circuit parts) are not shown.....	36

## **LIST OF TABLES**

---

Table 1: Key Performance Metrics for E-field Probe .....	15
Table 2: Impedance of Solenoid for Induced Electric Field Measurements .....	18

# 1 INTRODUCTION

---

Transcranial magnetic stimulation (TMS) is a commonly used tool in the academic study of the brain and for the clinical treatment of certain neuropsychiatric conditions [1]. In TMS a coil is positioned above a patient's head and driven with a sequence of current pulses, inducing a sequence of electric field pulses in a targeted region of the patient's brain, which subsequently modulate the neural activity there [2].

Given the targeted nature of its application a TMS coil's design is naturally predicated not only on the geometry of the coil but also on the geometry of the brain under stimulation, e.g. its size, its shape, and its underlying tissue layer composition [3]. As such computational simulation methods often play a significant role in the design of TMS coils. In fact, for the highest accuracy, simulation methods such as the boundary element method (BEM) as demonstrated by Nummenmaa [3] may be the best tool available for researchers and clinicians who need to accurately pinpoint the exact area of stimulation given a particular coil and target specimen.

Our computational capability will only improve with time. We should be wary, however, of believing too much in our models lest they lead us astray; as the old adage goes it is always good to trust but always better to verify. And in this spirit, the aim of this work is to add to the body of knowledge concerned with the physical measurement of coil performance. In what follows we demonstrate a way to measure the induced electric field distribution of a coil in air using an electrically small dipole antenna. This method has some advantages and some disadvantages compared with the methods and probes of prior work, whose operation we will briefly review before delving into the details of our approach.

## 1.1 PRIOR WORK ON ELECTRIC FIELD PROBES FOR TMS CHARACTERIZATION

As Makarov [4] explains the brain can be modeled as a weakly conducting medium satisfying the thin limit condition, i.e. the skin depth is much greater than the greatest dimension of interest of the object, and the general magneto-static approximation, whereby displacement current are neglected, for frequencies of interest for the object.

In neglecting displacement currents the relationship between current density,  $\vec{j}$ , and the magnetic field,  $\vec{H}$ , becomes:

$$\nabla \times \vec{H} = \vec{j} \quad (1)$$

whereas the electric field:

$$\vec{E} = -\frac{\partial \vec{A}}{\partial t} - \nabla \phi \quad (2)$$

must continue to be expressed in terms of both the magnetic vector potential,  $\vec{A}$ , and the electric scalar potential,  $\phi$ . Lastly, the eddy current,  $\vec{J}_s$ , is related to the electric field and bulk conductivity,  $\sigma$ , by:

$$\vec{J}_s = \sigma \vec{E} \quad (3)$$

The consequence of the thin limit condition with respect to TMS is that since the magnetic field due to the coil dominates any secondary fields created by eddy current, the electric field contribution due to  $-\partial A/\partial t$  in (2) is determined using coil current alone [4]. The contribution due to  $-\nabla \phi$  comes from charge accumulation at conductivity boundaries in tissue due to the eddy current flow [4].

Both contributions to the electric field as expressed in (3) are important for neuromodulation [5]. Therefore, in the review of prior work in the subsections that follow a distinction will be made between probes that can only capture the primary contribution to the electric field, or  $-\partial A/\partial t$ , and probes that can capture the complete electric field as describe in (2) and under what assumptions they do so.

The major types of probes that have been used to measure the electric fields patterns of TMS coils in the past are the following:

- a) electric field probes using bioelectrodes;
- b)  $\partial \vec{B}/\partial t$  probes using a small loop;
- c)  $\partial \vec{B}/\partial t$  probes using a long rectangular loop;
- d)  $\partial \vec{B}/\partial t$  probes using a triangular loop.

Among these only a) is designed to be used in tissue or saline solution-based phantoms, and only a) can measure the complete electric field of (1) under general conditions. The rest of the probes are meant to be used in air. The probes in b) and c) can only measure the primary electric field. The triangular  $\partial \vec{B}/\partial t$  probe of d) can be used to make a phantom measurement of the complete electric field found in a spherically symmetric volume conductor.

### 1.1.1 Bioelectrode-based Electric Field Probes

A bioelectrode is simply an electrode designed to be compatible for measurements in bodily tissues [6]. The free charge carriers in the metal conductor that makes up the electrode are electrons. The free charge carriers in bodily tissue are ions available in solution. The simplest model for a bioelectrode in an electrolytic solution is a built-in electric potential (a voltage source) in series with a parallel resistor and capacitor [6]. This voltage source is sometimes called the half-cell potential or the reversible potential [6]. The resistance is called the charge transfer resistance, or  $R_{CT}$ , and represents the change in the voltage drop across the electrode-electrolyte interface with current flow [6]. The capacitance is called the double-layer capacitance, or  $C_{DL}$ , and is reviewed in great detail by Bockris in [7].

Broadly speaking, there are two ways to apply bioelectrodes in measuring induced electric field during TMS. One method, called the loaded probe method [8], assembles two bioelectrodes to create an ammeter loosely speaking. The other method interfaces the bioelectrodes to a high impedance amplifier to create a voltmeter.

The most significant works using the loaded probe method in the evaluation of electric fields induced by TMS are those of Tay [9], [10], where TMS measurements were made in saline solution and in the brain of anesthetized cats. Although it is not precisely clear how Tay constructed her loaded probes based on her works alone, earlier works by Swiontek [8] and Deutsch [11] shed some light on nature of the construction. An illustration of Swiontek's loaded probe is shown in Fig. 1. In essence Swiontek proposes a probe whereby two opposite-facing sides of a small rectangular insulating volume are plated with a low  $R_{CT}$  bioelectrode surface that readily passes current to an external load resistance, which is matched to the electrolytic solution under test so that the probe in a way electrically transparent to the medium [8]. In other words, if the spacer thickness in Fig. 1 is  $d$  and the surface area of the low  $R_{CT}$  electrodes is  $A$ , then ideally the load resistance would be  $R_L = Ed/(JA)$ , where  $E$  and  $J$  are the electric field and current density normal to the low  $R_{CT}$  surfaces respectively. An interesting feature of the loaded probe is that the electrode surface area can be traded off for signal-to-noise ratio (SNR); i.e. assuming  $d$  is fixed,  $A$  can be increased and thereby  $R_L$  can be decreased reducing its thermal noise. One disadvantage is that the low  $R_{CT}$  surface shorts out the lateral electric field. Another disadvantage is that a large volume of the medium is potentially displaced by this electrode and that in a time-vary magnetic field the spacing between the electrode surfaces

might be problematic owing to the non-conservative nature of the magnetic field [12].

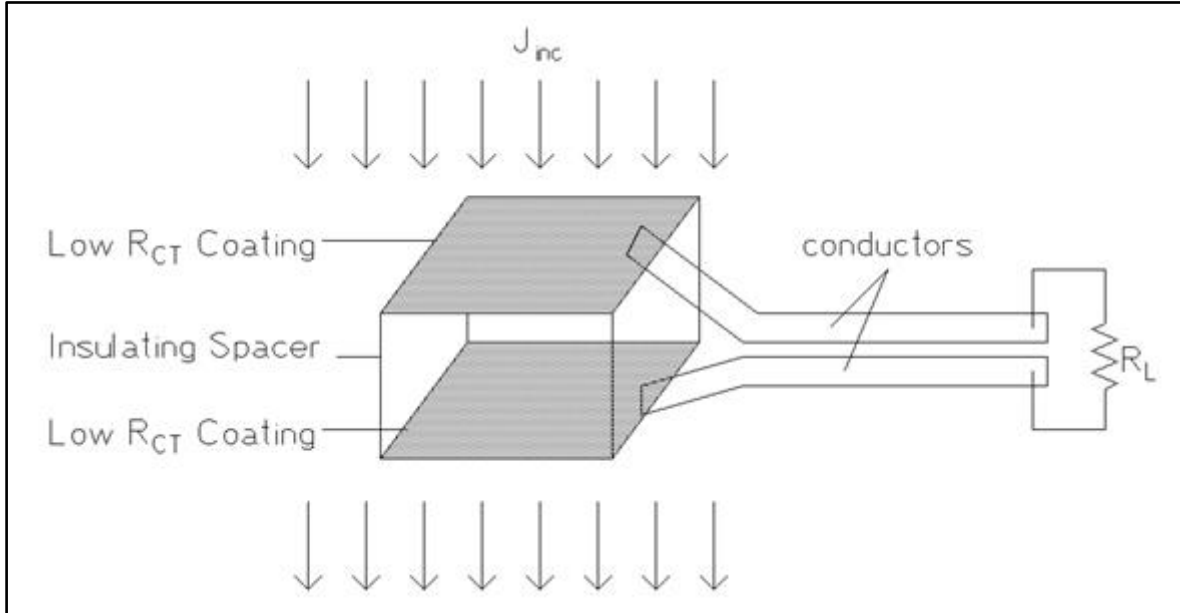


Figure 1: The following is a caricature of the loaded probe concept as proposed by Swiontek [8]. The bioelectrode surfaces normal to the current density being measured are processed to have a very low charge transfer resistance,  $R_{CT}$ . As such current readily enters the loaded probe forming a current divider with the medium. The load resistor is chosen to match the current density at the low  $R_{CT}$  surfaces of the probe with that of the medium.

The other popular method of constructing a bioelectrode-based probe is as a voltmeter so to speak. It is described so as the driving point impedance looking into the probe tips is designed to be high as the bioelectrode feedlines are ultimately interfaced to a high impedance voltage amplifier. Early references for this method can be found in the works of Durand [13], Tofts [14], Hart [15] and Maccabee [16]. In this method the bioelectrodes are formed in the shape of an electric dipole that maintains very close spacing between the feedlines [12].

One important requirement not explicitly stated in prior works on the short dipole probe is that the passive interface impedance of the bioelectrodes, e.g.  $R_{CT}$  in parallel with  $C_{DL}$ , should ideally be much lower than the input impedance of the downstream differential amplifier. This is because the passive interface impedance is not stable; both  $R_{CT}$  and  $C_{DL}$  can change with time, temperature, frequency and electrolyte concentration [17].

A second important requirement for the short dipole probe is that the feedlines must be routed together as closely as possible. The voltage seen by the downstream differential amplifier is the superposition of the voltage drop along the bioelectrodes due to (2) and the contributions of  $-\partial\vec{A}/\partial t$  along the feedlines. Since the magnetic field is non-conservative, exact cancellation of the feedline contributions can only occur if the feedlines are coincident in space as explained and demonstrated experimentally by Glover [12].

The greatest disadvantage with the bioelectrode-based approach, whether a loaded probe or short dipole probe is considered, compared with other approaches is that the experimental setup is the most complicated, primarily owing to the fact that it is a wet science. In principle, however, if a suitably detailed phantom can be built or in vitro measurements can be performed then accurate measurement of the complete electric field are possible, which is a claim no other probe of the prior art can make.

### 1.1.2 $\partial B/\partial t$ probes using a small loop

A small loop can be used to measure the magnetic field or flux. If the x, y and z components of the magnetic field over space are sampled properly, the inverse problem for the vector potential  $\nabla \times \vec{A} = \vec{B}$  could be solved. These probes can only measure the solenoidal electric field  $-\partial\vec{A}/\partial t$ . The advantage of small loop probes is that they are very easy to construct and that the measurements can be made in air. The disadvantage is that only the solenoidal electric field can be derived, and that three very small orthogonal loops and very many measurements are required to accurately restore the electric field.

### 1.1.3 $\partial B/\partial t$ probes using a long rectangular loop

Epstein [18] pioneered a clever rectangular loop probe to measure the solenoidal electric field without solving the inverse problem. His approach was successfully applied most recently by Salinas [19], [20], where he refers to the rectangular loop as a 3D eddy current probe. The basic construction of this  $\partial\vec{B}/\partial t$  probe consists of a long rectangular loop, whose long sides are determined by the amount of distance required for the magnetic vector potential to fall off to negligible levels [18]. The short sides are determined by the desired spatial resolution [18]. One short side is placed at the location and in the direction for the desired primary electric field measurement, while the other short side is connected to some voltage measuring devices like an oscilloscope [18]. If the long sides are centered along an axis of symmetry with respect to the magnetic vector potential, then the  $-\partial\vec{A}/\partial t$  contributions along the long sides cancel out and the total *emf* is simply the length of the short side multiplied by its  $-\partial\vec{A}/\partial t$ ; this is the voltage that is ultimately measured [18].

Tofts [14] criticized this approach for only being able to measure the solenoidal electric field along an axis of symmetry. However, that assessment is only true if a single measurement is permitted. Salinas [19] claims the design can be applied off of the axis of symmetry by using two measurements; however, it is not clear to me that his two-measurement technique is generally applicable. Unfortunately, Salinas was never contacted for clarification on his claim. The advantage of the rectangular loop is that measurements can be made in air and that it is relatively easy to construct. Salinas [20] suggested a simple way to create a two-axis probe using two orthogonal rectangular loops on a single support rod.

The advantage of the rectangular loop is that measurements can be made in air and that it is relatively easy to construct. The disadvantages of the probe are that it can only measure the primary electric field and it may only be able to do so along a line of symmetry where the  $-\partial\vec{A}/\partial t$  along the long sides cancels [18], [14]. I am not convinced of Salinas' claim [19] that with two measurements the unbalanced  $-\partial\vec{A}/\partial t$  contributions on the long sides can be compensated for, but let it be known that such a claim is out there.

### 1.1.4 $\partial B/\partial t$ probes using a triangular loop

The triangular loop-based  $\partial\vec{B}/\partial t$  probe was created by Niemenin [21]. His probe, which he called the TMS calibrator, was inspired by prior work done by Ilmoniemi [22], [23] on the inverse and forward problems of magnetoencephalography (MEG).

The basis for the operation of the Niemenin's TMS calibrator is a subtle argument that hinges on the fact that an externally applied magnetic field cannot induce a radial current in a spherical conductor [24]. Using this fact, a proof can be constructed to show that the external magnetic field generated outside of a

spherically symmetric volume conductor by an internal tangential current dipole and its associated volume currents is indistinguishable from that of a triangular current loop in free space that includes the original primary current dipole and whose vertex is the center of the original volume conductor [21]. Once this is proved it can be argued by reciprocity that the *emf* measured by the triangular loop so constructed is the same as the complete electric field integrated along the aforementioned tangential length in a spherically symmetric volume conductor [21]. An elegant graphical proof of this can be found in Niemenin's paper [21].

The advantages of Niemenin's triangular loop probe are that it is easy to construct and its measured *emf* is a phantom for the complete electric field at point inside a spherically symmetric volume conductor. Furthermore, Niemenin's triangular loop-based probe can be used in air. Its main disadvantages are that it cannot be used as a phantom for general volume conductor shapes or arbitrary conductivity profiles. One final disadvantage, albeit minor, is that a given triangular probe can only be used to sweep the electric field at a fixed radial distance. If a different sweep radius is desired the probe's vertex cannot simply be shifted in space, instead a new triangular probe with shorter radial side lengths must be constructed [21].

## 1.2 OTHER PRIOR WORK ON PROBES FOR EM FIELD MEASUREMENTS

### 1.2.1 Small Dipole with Capacitive Load

In a review of standard probes for electromagnetic field measurements, Kanda [25] discusses the idea of an electrically short dipole loaded with a capacitive load. Due to its capacitive self-impedance, the electrically short dipole antenna will yield a frequency independent transfer characteristic when driving a capacitive load. Kanda [25] experimentally demonstrates this feature using a 15-cm dipole (6-mm radius) connected to a 13 pF FET amplifier to achieve a flat frequency response from 2kHz to 400MHz.

The low frequency cutoff of this E-field probe is determined by the RC time constant made between the input resistance of the FET amplifier working against the combined input capacitance of the FET amplifier together with the antenna capacitance of the dipole. The high frequency cutoff is fundamentally limited by the half-wave resonant frequency of the dipole. The dipole must be operated below its half-wave resonant frequency in order to be considered electrically small so that its impedance remains predominantly capacitive. One easy way to extend the high frequency cut off is to use a physically smaller dipole. The tradeoff here is between bandwidth and signal-to-noise ratio as explained by Smith [26]. Another limitation at the time that Kanda wrote his paper [25] was the unavailability of differential FET amplifiers with adequate high frequency common-mode rejection. To extend the frequency range further the FET amplifiers would have to be replaced with a diode detector as describe in section 1.2.2, but this is a whole different animal as it is no longer able to measure the time-domain evolution of the E-field [25]. The beauty of the original approach is the time-domain behavior can accurately be measured as long as the spectra is contained within the bandwidth of the E-field probe.

The end application of Kanda's capacitively loaded small dipole antenna was in the measurement of EMI and EMC problems and determination of safe levels for electromagnetic radiation [25]. In recent years, other researchers have continued to use electrically small dipoles to create E-field probes for EMC and EMI test purposes [27], [28]. The most exciting new research I have found in this sphere is by Schmid & Partner Engineering AG (SPEAG) in Zurich, Switzerland, whereby they combined the electrically small, capacitively loaded dipole with an optical power and data link resulting in a fully robotized system that is able to sweep out the field in the vicinity of a device-under-test (DUT) for EMC/EMI characterization [29].

### 1.2.2 Small Dipole with Diode/Thermocouple Loads

To extend the high frequency range of the E-field probes discussed in section 1.2.1 the FET amplifier of the last section can be replaced with a diode or thermocouple detector. This system is a whole different animal from the E-field probes discussed in the last section. For starters the probe is no longer able to accurately measure pulse waveforms in the time domain. It either outputs a signal proportional to the square of the electric field magnitude or the peak depending on the signal level [25], [30]. As such the probe is designed to be used as a DC instrument, whose output is ultimately connected through a DC voltmeter.

In the case of the diode load the reason for this behavior is owed to the non-linear I-V characteristic of the diode and its relative slow response time relative to the RF signal from the antenna. As a result of these two characteristics, when given a continuous wave (CW) signal the diode will be driven into its reverse-bias region as the junction capacitance is much lower when the diode is reversed-biased, meaning the negative going pulse will have a much easier time driving the diode's junction capacitance than that of positive going pulse. If the amplitude of the input signal is large the diode will be driven deeper into reverse bias where its junction capacitance becomes more linear. This is the region where the probe output is proportional to peak signal level. With low input signal levels, the diode is biased close to its zero bias point. Owing to this fact the probe's output now has a square-law dependence on the input field [25]. Details on the operation of the small dipole with a thermocouple detector is explained by Bassen [30].

The last detail I would like to mention about this class of E-field probes is that since they are designed to only measure the magnitude or the square magnitude of the electric field the dipole is interfaced to the downstream instrumentation via a very resistive transmission line to filter out the RF signal content and to minimize the extent to which the probe scatters the incident field as explained by Bassen [30]. In particular, Bassen [30] explains the high resistance transmission line can be formed using carbon impregnated Teflon strips with resistivity of 4 megaohm/meter.

### 1.2.3 Electro-optic Probes

Electro-optic (EO) probes use the fact that an applied electric field changes some optical properties of an EO material in order to indirectly infer the electric field by measuring the change in the relevant optical properties [31]. Jarrige [31] developed an EO probe suitable for bioelectromagnetic investigation over a frequency range from 1KHz to 10GHz. His probe is able to extract the vectorial electric field and was an extension of prior work completed by Wakana [32] and Bernier [33]. The use case for these probes seems to be in the measurement of specific absorption rates (SAR) of electromagnetic radiation; in fact, Jarrige [31] claims that his EO crystal has a relative permittivity of 42, which he implies makes it a good candidate for testing of biological media, which has a similar relative permittivity at a frequency of interest, meaning that the crystal should be transparent to the environment in which it is submerged. Zhu [34] claims that the one drawback to electro-optic technology is that the EO materials can have piezoelectric properties, which limit low frequency operation to tens of kilohertz.

Given the discussion in the previous paragraph it seems that EO probes are likely competitors to the small dipoles loaded with diode detectors described in section 1.2.2. One obvious drawback I see to the EO probes described in the works of Jarrige [31], Wakana [32] and Bernier [33] is the high computational and optoelectronic overhead required for its operation.

### 1.3 CONTRIBUTION OF THIS WORK

From section 1.1 we see that there was and still is interest in being able to evaluate electric field measurements of TMS coils in air. This is probably partially due to the fact that air is a more controlled medium than saline solution, which makes air the better candidate for making meaningful comparisons between measurements and simulations (i.e. there may be less guesswork involved with air as the medium.) Furthermore, owing to the relative simplicity of air as a test medium compared to saline solution, the automation of in-air electric field measurements should in principle be more easily accomplished. In fact, Niemenin [21] constructed a fully robotized measurement system utilizing his triangular loop that was able to sweep out the electric field pattern on a hemispherical surface with the push of a button.

The trouble with loop-based approaches is that they in general cannot measure the complete electric field, including the contributions from both the electric scalar potential due to surface charges and the magnetic vector potential due to the coil current. This is simply due to the fact that the  $-\nabla\phi$  contribution comes from surface charge accumulation normal to the eddy current density in a medium of varying conductivity; in other words, without the actual volume conductor (e.g. saline solution) there are no eddy currents and hence no induced surface charges and hence zero  $-\nabla\phi$ . Niemenin's approach [21] using the triangular loop represents the best method known to date for measuring the electric field of a TMS coil in air. Its only drawback is that the conditions under which the *emf* picked up by his triangular loop is proportional to the field around a tangential current dipole (including both the primary and secondary field components) are that the volume conductor be perfectly spherically symmetric; note that this spherical symmetry does allow conductivity to vary radially [21]. These conditions limit the general-purpose applicability of Niemenin's probe because the brain, even if limited to cranial cavity is not perfectly spherical and the conductivity profile is not always perfectly radial [3]. With small deviations in the spherical symmetry of the volume conductor the prevailing belief that the TMS coil cannot induce radial currents is no longer true as explained in detail by Mosher in his *Review on the Importance of Volume Currents* [35]. All of this said in no way should diminish the great utility of Niemenin's probe as a calibration instrument; with it numerical simulation of coils and spherical conductor models can be validated against accurate, in air measurements, which is truly remarkable [21].

To measure the complete electric field the bioelectrode-based approach of section 1.1.1 is the only way known to date. The loaded probe approach is of limited applicability in my opinion due to the non-conservative nature of the magnetic field and to the fact that lateral electric fields can be shorted out by the low RCT surface electrodes as was discussed in section 1.1.1. The best approach is the short dipole probe owing to its high impedance, which should minimally distort the field distribution in the medium, and the close spacing of the feedlines, which should minimize  $-\partial\vec{A}/\partial t$  along the feedlines as explained by Glover [12]. The largest drawback with the bioelectrode-based approach is the saline solution or tissue medium, which would seem to require a lot of experimental due diligence to make sure experimentation is controlled.

In this thesis I propose to add a new probe for the measurement of electric fields of TMS coils. This probe is simply the electrically short dipole antenna loaded with a capacitive load that was presented in section 1.2.1 but adapted for the evaluation of TMS coil performance. Its unique features include high spatial resolution, large frequency band from 100 Hz to 300 kHz, efficient feedline isolation via a printed Dyson balun, and good signal-to-noise properties. In this thesis I demonstrate how the probe can be used to measure induced electric field pattern (due to  $-\partial\vec{A}/\partial t$ ) of a coil in air. I also demonstrate how the probe can be used to measure the electric field pattern (due to  $-\nabla\phi$ ) of a parallel-plate capacitor. Data for the frequency and time-domain characterization of the probe is also presented.

In the context of the TMS probes of prior works the probe of this thesis is able to generally measure the primary field component in air with a single measurement, which represents an improvement over the rectangular loop. Furthermore, it should in principle be applicable in the measure of the complete electric field inside saline solution phantom or tissue sample. This is not demonstrated in this work but is further discussed in the conclusion.

## 2 ELECTRICAL DESIGN AND IMPLEMENTATION

In this section I will review in detail the design of the electrically small dipole probe of this thesis, which will be referred to as the E-field probe from here on out. The E-field probe consists of a small dipole as shown in Fig. 2a whose feedlines are capacitively coupled to the inputs of an optically isolated instrumentation amplifier via a printed version of the Dyson balun [36], [37]. At face value the circuits involved are not particularly challenging or difficult, which is great from an engineering perspective; however, there are some subtleties related to the interplay between biasing, spatial resolution, frequency range and signal-to-noise ratio, which I will discuss in the sections that follow.

I will first start by describing the implementation of the dipole and balun. Then I will present the instrumentation, including hardware that goes beyond the core circuits shown in Figure 2c for the reader interested in reproducing the probe of this work. With the hardware sufficiently described I will discuss the design tradeoffs between spatial resolution, frequency range, biasing and the signal-to-noise ratio. In the final section I will summarize the key performance metrics of the hardware implementation that was ultimately realized.

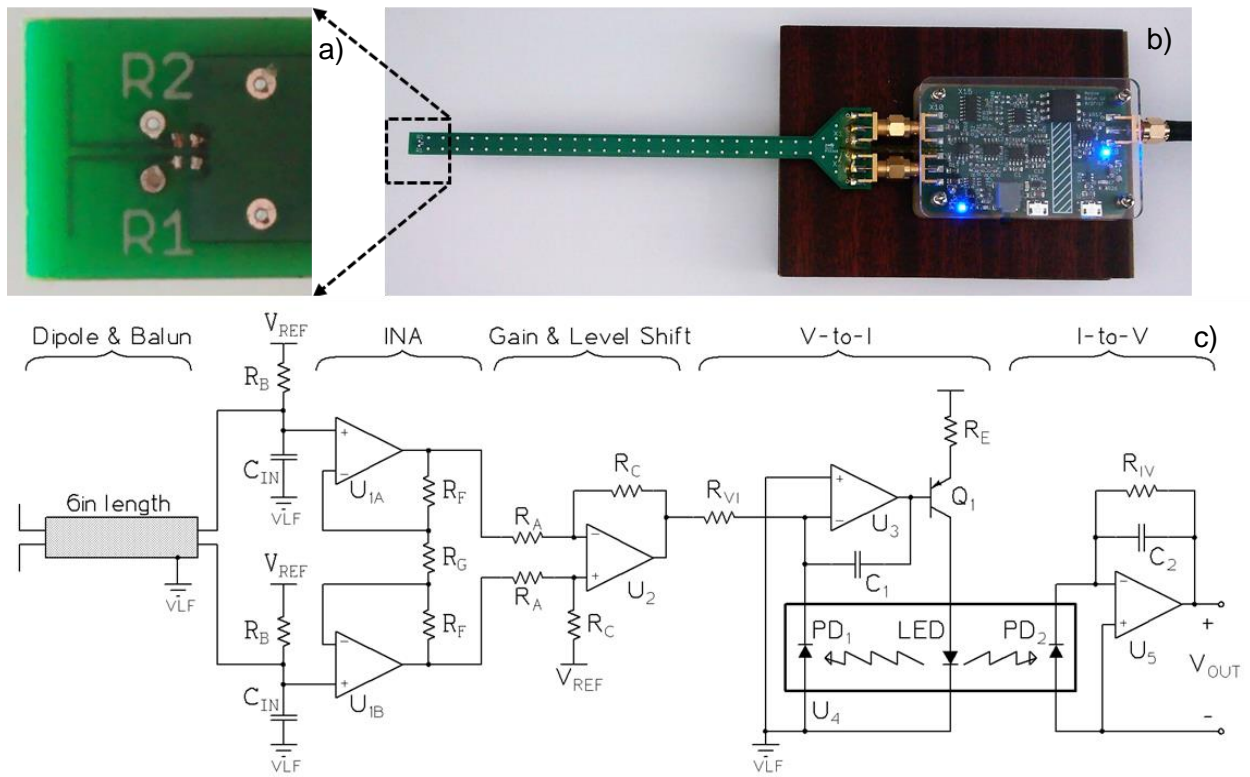


Figure 2: a) – Zoom-in of the 5mm printed dipole; b) – the dipole, balun and instrumentation assembled together; c) – a simplified schematic for the complete electric field probe; biasing and other ancillary circuitry are omitted.

### 2.1 DIPOLE AND BALUN HARDWARE

The dipole and balun were implemented using a standard 4-layer, 0.062” FR4-based PCB with stack-up

shown in Figure 3. To implement the printed, Dyson balun, which is equivalent to a shielded, balanced two-conductor transmission line, only three layers are really necessary; the 4-layer structure was chosen as it is inexpensive and easy to manufacture given the desired 0.062” total thickness. Although the resultant stack-up is not symmetric with respect to the cross-section it is balanced with respect to the feedlines, which is the key feature. The 0.062” thickness was driven by the desire to interface standard edge-mount SMA connectors to the final assembly. Figure 4 shows the top view of the dipole and balun PCB. Layers 1,3 and 4 of the PCB were exclusively used as the shield and were stitched together with vias spaced 0.2” (or 0.508cm) apart on either side of the feedlines. The dipole and the feedlines were routed on inner layer 2 using 7mil (or 0.178mm) thick traces. The dipole length was 5mm and the gap between the feedlines was 8mils (or 0.203mm). The total feedline length was 6” (or 15.24cm).

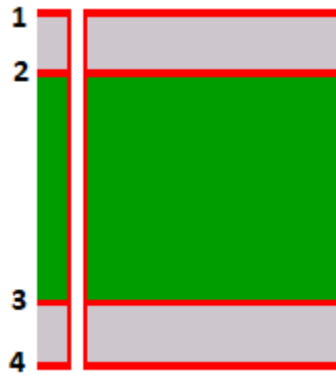


Figure 3: Stackup for PCB of dipole and balun. Copper layers are 1 oz. thick (1.35mils). Prepreg thickness between layers 1-2 and layers 3-4 is around 9.5mils. Thickness of center core material between layers 2-3 is about 39mils.

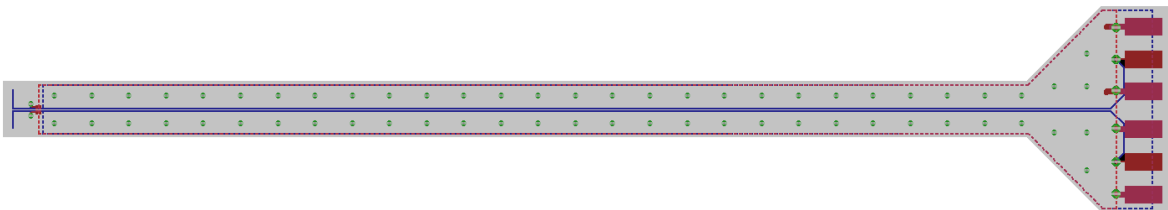


Figure 4: Top view of PCB for dipole and balun. Dipole and feedlines are shown on layer 2. Layers 1,3, 4 are the shield of the balun. The layers are stitched together with the vias denoted as green dots.

The feedlines of this PCB are ultimately interfaced to a separate PCB where the instrumentation resides. The separation of the dipole/balun from the instrumentation was so chosen to save on material costs in anticipation of the iterative nature of electronics design; the idea was that it would be wasteful to do a re-spin of the complete structure if only a small revision were required for one part. No good deed goes unpunished, however, as the two PCBs required a SMA connector bridge as shown in Figure 2b, which was a source of unwanted  $\partial \vec{B} / \partial t$  coupling during the solenoidal field testing, which is further discussed in Section 4.4. In order to eliminate the parasitic  $\partial \vec{B} / \partial t$  coupling the feedline traces were ultimately cut on either end of the SMA connector bridge as shown in Figure 5 and routed back along the same path they came before jumping the gap by way of a differential pair made using AWG32 magnetic wire. In this case the role of the SMA connector bridge was reduced to mechanical support and shield biasing.

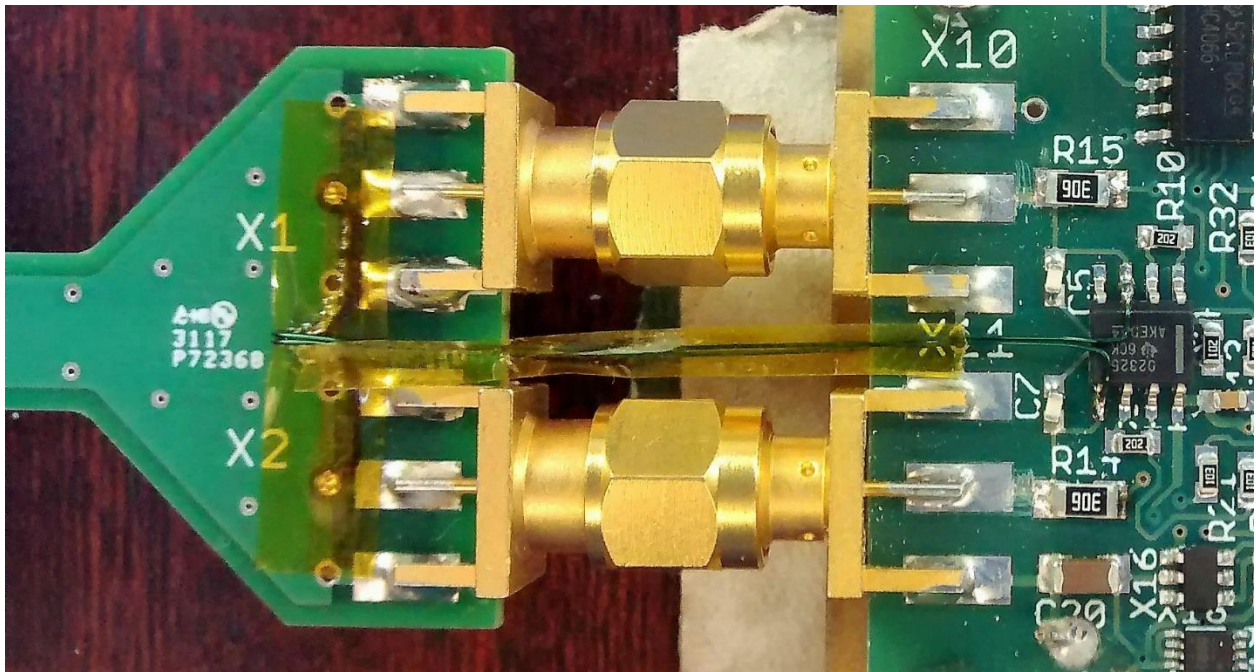


Figure 5: Photograph showing the rework needed to eliminate the loop made by the SMA connector assembly required by the partitioning of the design into two PCBs. The feedlines are cut on the top layer before they reach the pads for the SMA center conductors on both the dipole/balun PCB and the instrumentation PCB. The feedlines are routed through air using a differential pair made using AWG32 insulated wire.

## 2.2 INSTRUMENTATION HARDWARE

The instrumentation PCB was implemented using 2-layer, 0.062" FR4 stack-up with top and bottom layer plated to 1oz. copper. The artwork for the design is shown in Figure 6. As the instrumentation is optically isolated there are two separate ground planes for the floating circuits, which interface to the dipole/balun, and the grounded circuits, which ultimately interface with an oscilloscope. The shield of the balun is connected to the floating ground. The ground of the grounded circuits is connected to the outer conductor of the output SMA connector, meaning that it will ultimately be connected to the oscilloscope ground. The split between the two ground planes is denoted by the diagonally striped pattern in Figure 6.

The essential circuits comprising the instrumentation were already depicted Figure 2c), where it is also noted that biasing and other ancillary circuits are omitted. The large volume of circuitry evident in Figure 6 is in large part due to the aforementioned biasing and ancillary circuits. As the operation of these additional circuits is not particularly relevant to the operation of the E-field probe they will not be discussed in depth in this section. The only significant thing to appreciate with respect to the additional circuits are that they pertain to battery power operation, a simple push-button state-machine and an optional high-pass filter for 60Hz suppression (intended as a debug mode.) For information on the ancillary circuitry refer to Appendix A.

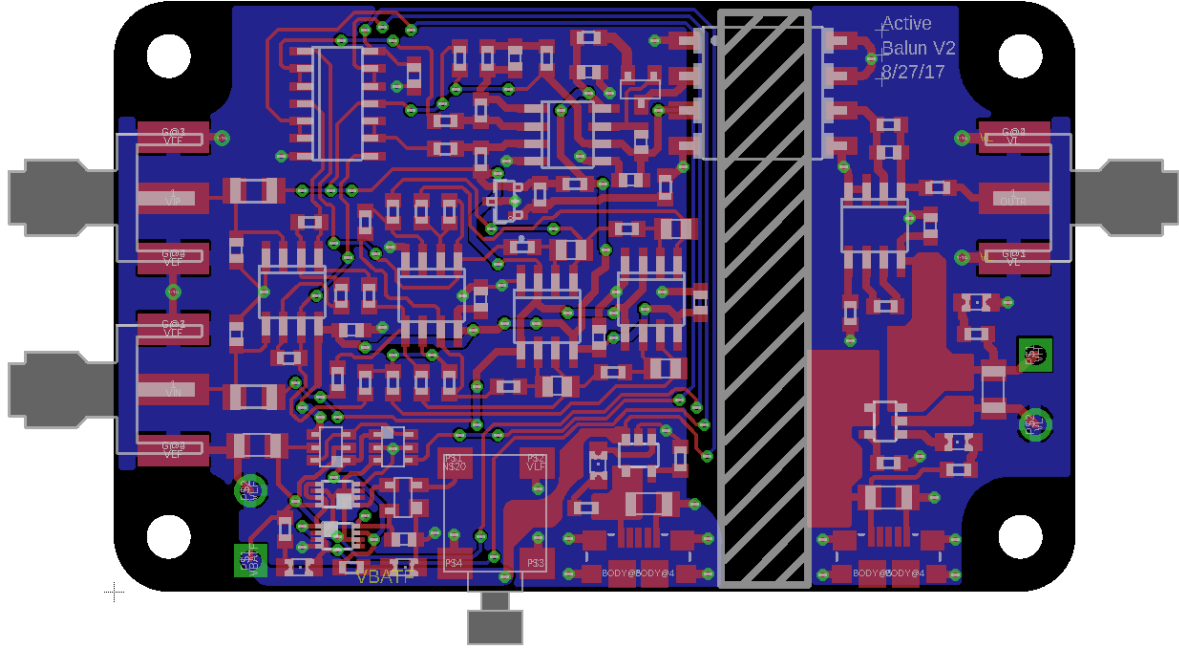


Figure 6: PCB artwork for the 2-layer, 0.062” FR4-based PCB for the instrumentation. The bottom layer (blue) is mainly used as ground plane. The top layer (red) is used for routing. The split between the floating and grounded sides of the optical isolation boundary is illustrated using the diagonal strip pattern in the silk-screening.

## 2.3 DESIGN PROCESS AND TRADEOFFS

As the dipole described in section 2.1 is self-resonant at 30 GHz (in air,) its antenna impedance is purely capacitive around 3 kHz (e.g. the center frequency for TMS) with virtually zero radiation resistance. To achieve a broadband, frequency independent gain characteristic between input field and the measured signal the only option is to present a capacitive load to the feedlines as Kanda demonstrated in prior work [25]. While Kanda interfaced his dipole feedlines to a RF FET differential amplifier, this design will operate solely in the frequency range of electrostatics, and so I am able to utilize simple voltage op-amps to achieve great linearity and accuracy. And so, for this probe’s design, the dipole feedlines were simply interfaced to the inputs of an instrumentation amplifier (INA).

If the inputs to the instrumentation amplifier are only interfaced to the feedlines the bias point will be indeterminate practically speaking. The feedlines would find a DC bias point, but this point would be determined by printed circuit board leakage paths, op-amp input bias currents and board contamination/cleanliness. To properly establish a bias voltage on the inputs of the instrumentation amplifier and feedlines a bias resistor is needed. With a bias resistance, e.g.  $R_B$  in Figure 1c), as high as 500 M $\Omega$  functionality was confirmed but a sensitivity to solder flux residue was observed in my testing.  $R_B$  was ultimately chosen to be 30M $\Omega$  for the final design.

As the dipole antenna capacitively couples into the inputs of the INA, as previously discussed, the low frequency cutoff,  $f_{LOW}$ , is equal to  $(2\pi R_B C_{TOT})^{-1}$ , where  $C_{TOT}$  is made up of double the antenna’s impedance, double the differential line-to-line capacitance of the two-conductor transmission line, the

whole line-to-shield capacitance of the two-conductor transmission line, the common-mode input capacitance of INA op-amp, the parasitic shunt capacitance of  $R_B$ , and any additional external input capacitance  $C_{IN}$ . The additional input capacitance  $C_{IN}$  is a degree of freedom for lowering  $f_{LOW}$ . At the same time,  $C_{IN}$  also attenuates the input signal resulting in a degradation of the SNR.

The SNR of the system is determined by the INA input stage alone. Downstream stages do not contribute into the noise calculation due to the high gain of the INA, which should be set as large as possible given bandwidth and accuracy requirements: in our implementation it was set to 20 V/V, which reduces the closed loop bandwidth of our selected op-amp to 500 kHz. The noise contributors are the equivalent noise voltage and equivalent noise current of the INA op-amps,  $e_n$  and  $i_n$ , respectively, and the thermal noise from  $R_B$  shown in Fig 7a. It is assumed that INA feedback resistors,  $R_G$  and  $R_F$ , shown in Fig. 2 are chosen such that their noise contributions are negligible.

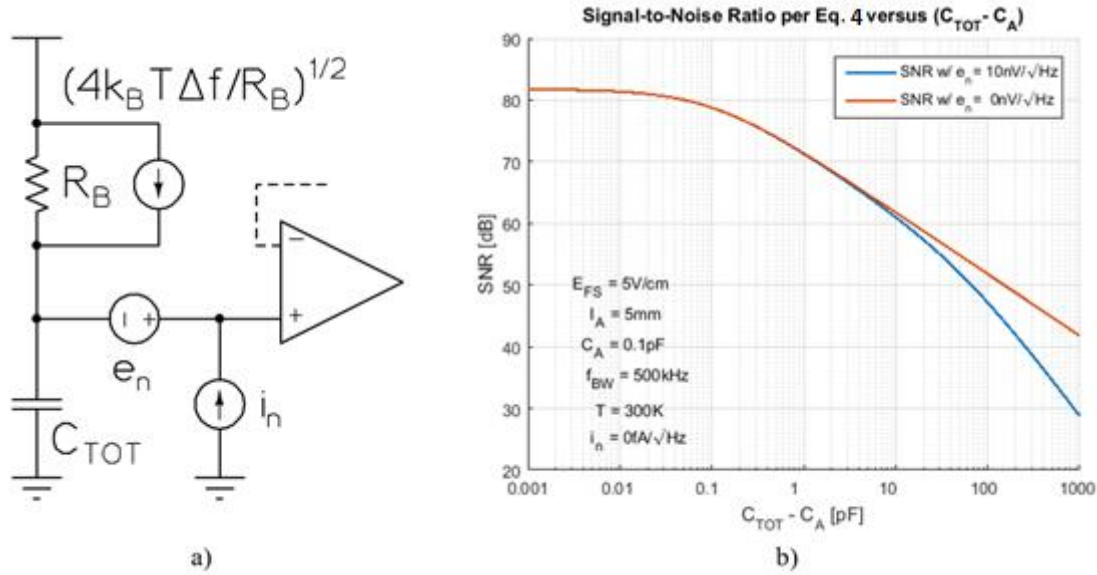


Figure 7. a) – Simplified INA half-circuit noise model; b) – computed signal-to-noise ratio following Eq. (1); note that  $i_n$  is set to 0 for these calculations.

The total input referred noise is approximately given by  $\sqrt{(\pi/2)f_{BW}e_n^2 + k_B T / C_{TOT}}$ , where  $f_{BW}$  is the bandwidth of the INA op-amp,  $k_B$  is Boltzmann's constant and  $T$  is the absolute temperature in Kelvin. Even with  $R_B=30\text{M}\Omega$  the noise contribution from  $i_n$  turns out to be negligible compared with that of  $e_n$  for the OPA2325, which was the op-amp ultimately used and thus  $i_n$  was omitted in the noise expression. The input signal is determined by the full-scale input field  $E_{FS}$ , the dipole length  $l_A$ , and the capacitive divider made between the half-circuit antenna capacitance  $C_A$  and  $C_{TOT}$ . The expression for the resultant SNR is obtained in the form:

$$SNR = 20 \log_{10} \left( \frac{E_{FS} l_A C_A}{C_{TOT} \sqrt{(\pi/2) f_{BW} e_n^2 + k_B T / C_{TOT}}} \right) \quad (4)$$

A plot of Eq. 4 versus  $(C_{TOT} - C_A)$  is shown in Fig. 7b. The SNR of the system using the OPA2325 with  $e_n = 10 \text{ nV}/\sqrt{\text{Hz}}$  is shown in blue and the SNR of a system using a noiseless amplifier is shown in red; the difference between the curves is the noise figure of our circuit. In order to minimize this noise figure (i.e.

keep it less than 5dB) we should keep  $C_{TOT}$  less than 100 pF. We also see that the SNR of our system falls off at two different slopes. When  $C_{TOT}$  is less than 20 pF but greater than 0.1pF the SNR degrades at a rate of 10 dB/decade; whereas, when  $C_{TOT}$  is greater than 20pF the SNR degradation slope becomes 20 dB/decade. This difference in slopes is due to the fact that the noise power saturates to a constant level determined by  $e_n$  alone when  $C_{TOT}$  is greater than 20 pF, whereas the noise power decreases at a rate of 10 dB/decade when  $C_{TOT}$  is less than 20 pF. The plateau seen at minimal ( $C_{TOT} - C_A$ ) can be understood analytically by taking the limit of Eq. (2) as  $C_{TOT} \rightarrow C_A$ . Since the self-capacitance of an electrically small dipole is proportional to its length  $l_A$  [25] we can replace  $C_A$  in our expression with  $\kappa l_A$ , where constant  $\kappa$  has units of F/m and is the first coefficient of the power series expansion, and neglect the contribution from  $e_n$  altogether, which yields

$$\lim_{C_{TOT} \rightarrow C_A} SNR = 20 \log_{10} \left( \frac{E_{FS}}{\sqrt{k_b T}} \sqrt{\kappa} (l_A)^{3/2} \right) \quad (5)$$

Eq. (5) illustrates a tradeoff between the spatial resolution and the maximum achievable SNR. For a given dipole length,  $l_A$ , the only means to improve the SNR is to increase the full-scale electric field or to decrease temperature. The derivation presented here is simplified; a more detailed derivation of a similar system can be found in [26].

The design of the rest of the system is less critical and I will present it expeditiously. The instrumentation amplifier gives us a differential output. A single-ended output and more gain is ultimately needed to interface with the HCNR201. To accomplish this, a simple difference amplifier was used to do the differential to single-ended conversion.

The last part of the design is galvanic isolation via the Broadcom HCNR201 matched opto-coupler shown in Fig. 2c. The purpose of the galvanic isolation is to suppress any common-mode current. The optical isolation amplifier of Fig. 2c depends on tight matching of photodiodes  $PD_1$  and  $PD_2$  and equal illumination by the LED, which is guaranteed by the design of the HCNR201. The first op-amp drives the PNP and ultimately the LED to make the current in  $PD_1$  and  $PD_2$  equal to  $V_{IN}/R_{VI}$ . Hence the output voltage,  $V_{OUT}$ , will be equal to  $V_{IN}$  to within the bandwidth of the cascade of amplifiers, which is set by  $C_1$  and  $C_2$ .

Both sets of circuits, on either side of the isolation barrier, are battery powered to eliminate any potential common-mode noise issues.

## 2.4 FINAL DESIGN PARAMETERS

Figure 8 shows the simplified schematic for the complete electric field probe repeated from Figure 2 for the reader's convenience; biasing and other ancillary circuitry are omitted. The dipole-facing and output facing circuits are galvanically isolated via  $U_4$  and separate batteries are used to supply the bias power. The component values used for the final implementation are:  $R_B = 30 \text{ M}\Omega$ ,  $C_{IN} = 22 \text{ pF}$ ,  $R_F = 2 \text{ k}\Omega$ ,  $R_G = 200 \text{ }\Omega$ ,  $R_A = 1 \text{ k}\Omega$ ,  $R_F = 15 \text{ k}\Omega$ ,  $R_{VI} = 82 \text{ k}\Omega$ ,  $R_{IV} = 82 \text{ k}\Omega$ ,  $R_E = 50 \text{ }\Omega$ ,  $C_1 = 10 \text{ pF}$ ,  $C_2 = 5 \text{ pF}$ ,  $Q_1 = \text{ON Semiconductor BC856}$ . All resistors excepting  $R_E$  and  $R_B$  should be 1% tolerant (preferably 0.1%).  $C_{IN}$  should match to better than 1pF and utilize a Class 1 dielectric (e.g. preferably NP0). All op-amps were implemented using the Texas Instruments OPA2325;  $U_{1A}$  and  $U_{1B}$  must be co-packaged. The Broadcom HCNR201 was used to implement the matched opto-coupler depicted with  $U_4$ .  $V_{REF}$  was pinned to 1.8V above VLF and was developed using the Texas Instruments TLV431B shunt regulator. The net label VLF represents the return

of the antenna-facing floating circuits.

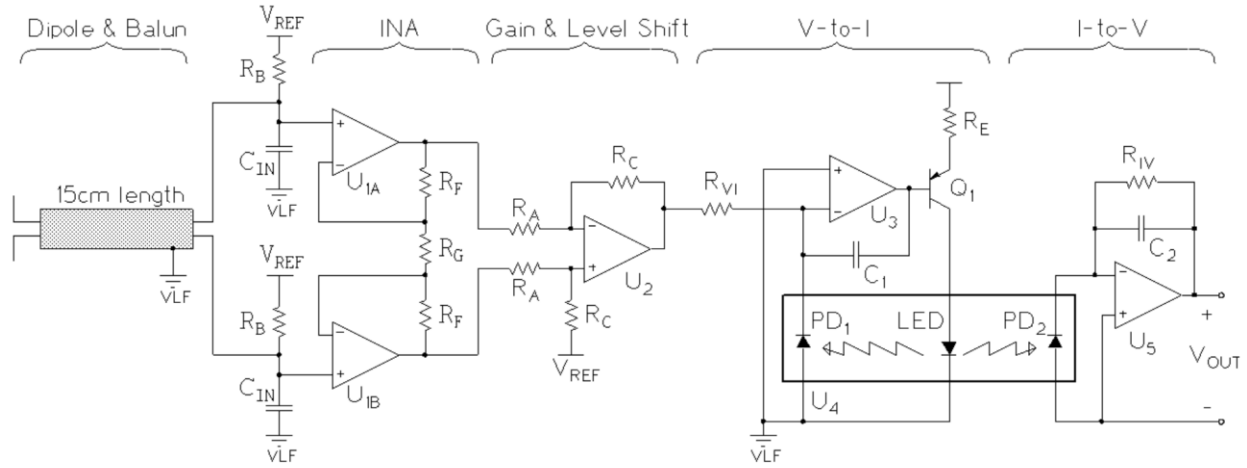


Figure 8: This is a repeat of Figure 2c) to improve the readability of this section

The summary of some key performance metrics can be found in Table 1. Data supporting the claimed frequency range and common-mode rejection can be found in Section 4.1. Common-mode rejection is defined as the amount of rejection of floating ground variation by the output port (e.g. 50dB corresponds to a rejection factor of 316, meaning that 1V of variation on the floating ground results in 3.16mV of variation on the output port). The spatial variation is determined by the dipole length alone. The probe conversion factor relates the variation in probe output voltage to incident electric field as determined by a parallel plate calibration setup described in section 3.3 (e.g. 1V/cm of input field variation should show up as 0.227V of variation on the output port.) The input dynamic field range was determined based on oscilloscope waveforms and the compliance of the active circuitry. In other words, a variation of 50mV/cm of incident electric field was observed to be clearly discernable as approximately 10mV on an oscilloscope with no averaging (e.g. refer to section 4.4); The active circuitry is designed to swing +/-1.5V on the output, which limiting the maximum input dynamic range for the field to +/-6.6V per cm. The quiescent current is equally split between the bias current required for the HCNR201 LED, which is approximately 4mA, and the bias current required for the six op-amps used in the instrumentation each of which consume 0.65mA. The peak working voltage is determined by the insulation ratings of the HCNR201 opto-coupler.

TABLE 1: KEY PERFORMANCE METRICS FOR E-FIELD PROBE	
SPECIFICATION	TYPICAL VALUE OR RANGE
Frequency Range (kHz)	0.1-300
Common-mode Rejection @ 3kHz (dB)	50
Spatial Resolution (mm)	5
Probe Conversion Factor (V per V/cm)	0.227
Input Field Dynamic Range (V/cm)	0.050 - 6.6
Quiescent Current (mA)	8.3
Isolation Peak Working Voltage (V)	1414
Battery Technology	Lithium-Ion 400mAh
Battery Charging Method	Micro USB 5V powered LDO

## 3 EXPERIMENTAL PROCEDURES AND SETUP

---

In this section the experimental procedures and setup are described. Section 4 discusses the results of the measurements and presents the data. Section 3.1 describes the differential and common-mode frequency responses, which were determined using a network analyzer. Section 3.2 describes the experimental setup for the transient response measurements. Section 3.3 describes the experimental setup for the evaluation of the probe's ability to measure electrostatic electric fields using a parallel plate capacitor setup. Finally, section 3.4 describes the experimental setup for evaluating the probe's ability to measure solenoidal electric fields due to Faraday's law of induction alone.

### 3.1 FREQUENCY RESPONSE

This section describes the experimental procedure and measurement setup for the evaluation of the differential-mode and common-mode gains.

#### 3.1.1 Differential-mode Gain

The differential mode gain was measured using the parallel plate capacitor setup described in Section 3.3 together with the AP instruments AP300 network analyzer. The dipole feed of the electric field probe was positioned in the center of the capacitor test setup with the dipole wings aligned along the axis of symmetry. The top plate of the capacitor test setup was connected to both the injection source and the input channel (i.e. A) of the network analyzer. The output port,  $V_{OUT}$ , of the electric field probe was connected to the output channel (i.e. B) of the network analyzer. The bottom plate of the capacitor test setup and the outer conductors of all coaxial cables used (for the injection source, input channel A and output channel B) were connected to the return of the output port,  $V_{OUT}$ , of the electric field probe. The output power of the injection source was set to 7dBm, corresponding to a voltage amplitude of 0.5V across the plates of the capacitor test setup. The frequency of the injection source was swept from 10 Hz to 1 MHz, and both the gain and phase of chosen network (i.e. B/A) were measured.

#### 3.1.2 Common-mode Gain

The common-mode gain was evaluated using the instrumentation PCB assembly alone with the Agilent 4395A network analyzer. The SMA connector inputs of the instrumentation PCB assembly were shorted together. Both the injection source and input channel (i.e. A) of the network analyzer were connected to the floating circuit return, VLF. The output channel (e.g. B) of the network analyzer was connected to the output port,  $V_{OUT}$ . The outer conductors of all coaxial cables used (for the injection source, input channel A and output channel B) were connected to the return of the output port,  $V_{OUT}$ , of the electric field probe. The output power of the injection source was set to 15dBm, corresponding to a voltage of 2.52V across the optical isolation barrier. The frequency of the injection source was swept from 100Hz to 1MHz, and both the gain and phase of chosen network (i.e. B/A) were measured.

### 3.2 TRANSIENT RESPONSE

The transient response was measured using the parallel plate capacitor setup described in section 3.3

together with an Agilent 33250A function generator. The dipole feed of the electric field probe was positioned in the center of the capacitor volume with the dipole wings aligned along the axis of symmetry. The top plate of the capacitor test setup was connected to function generator output. The bottom plate of the capacitor test setup and function generator return were connected to the return of the output port of the electric field probe. The load impedance setting of the function generator was set to high impedance. The square wave function was used to drive function generator output at an amplitude of 10V. The output port of the electric field probe was connected to a Tektronix MSO4000B oscilloscope. Transient response waveforms given a function generator frequency of 100 Hz, 10 kHz and 100 kHz were captured.

### 3.3 QUASISTATIC ELECTRIC FIELD OF PARALLEL PLATE CAPACITOR

A parallel-plate, air-filled capacitor with plate separation distance of 4.128 cm, circular plate diameter of 10 cm, and plate thickness of 0.25 mm was constructed and positioned on a grid as shown in Figure 9. The plates of the test capacitor were driven by a bipolar function generator so that the potentials of the top plate and bottom plate were equal in magnitude but perfectly output of phase; the differential voltage amplitude across the plates was 7.6V; the frequency of excitation was 20 kHz; and the wave shape was sinusoidal. The output port of the electric field probe was connected to a Tektronix MSO4000B oscilloscope. The resultant constant wave (CW) electric field was measured at different points in space.

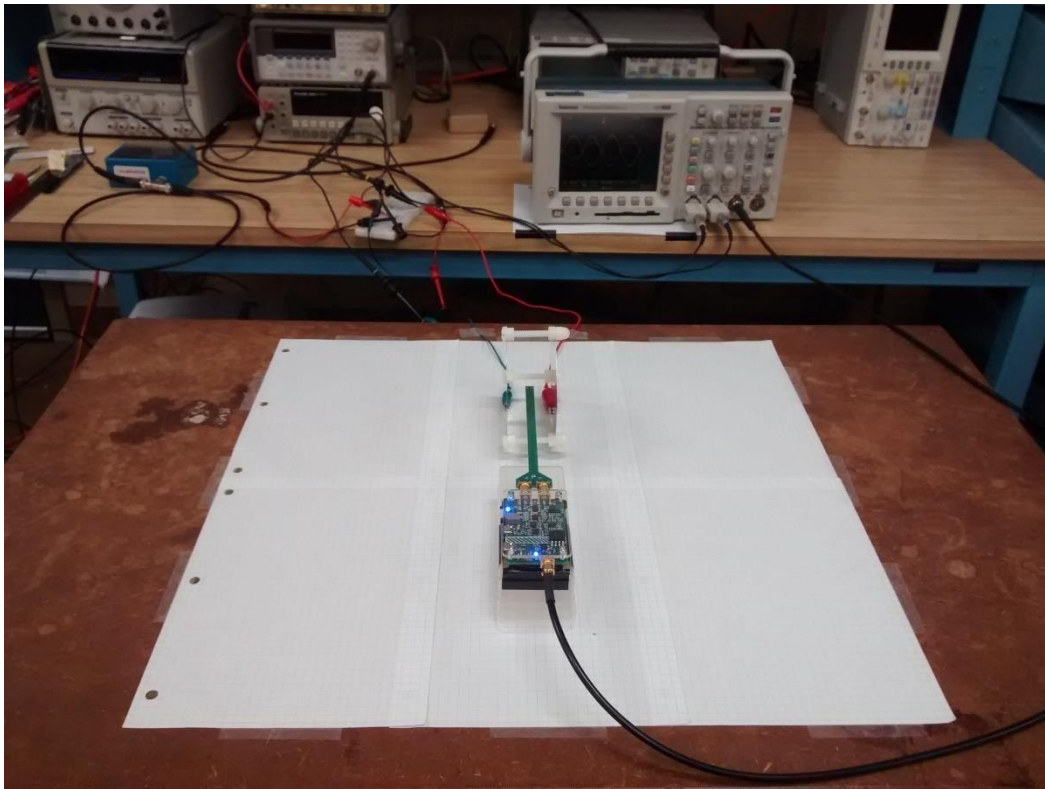


Figure 9: Parallel plate capacitor setup for parallel capacitor experiments.

### 3.4 QUASISTATIC ELECTRIC FIELD OF SOLENOID

A solenoidal coil is wound using AWG 18 copper magnet wire to make a 35-turn single layer solenoid with a diameter of 5.3cm and a length of 3.58cm. The impedance was measured with the HP 4284A

Precision LCR meter and is shown in Table 2.

TABLE 2: IMPEDANCE OF SOLENOID FOR INDUCED ELECTRIC FIELD MEASUREMENTS

Frequency (kHz)	Resistance (ohm)	Reactance (ohm)	Inductance (uH)
0.3	0.1400	0.1064	56.45
1.0	0.1364	0.3538	56.30
3.0	0.1380	1.0564	56.04
10	0.1495	3.5173	55.98
30	0.2168	10.514	55.78
100	0.4881	34.737	55.29
300	1.0015	103.44	54.88
1000	2.1080	343.75	54.71

The coil was inserted into a current stimulator described in Appendix B. To operate the coil stimulator a bias voltage is applied to its VBIAS port. The current pulse is initiated by pulsing the VFG port with a manually triggered 1us, 5V single-shot pulse using a pulse generator. To first order the resultant peak current pulse amplitude is given by:

$$i_{coil} \approx \frac{R_{F1}}{(R_{F1} + R_B)} \frac{V_{BIAS}}{\sqrt{L_{FLD}/C_{RES}}} \quad (6)$$

A sheet of acrylic measuring 8½”x11” was coated with a layer of aluminum foil on one side to create a shield. The shield was positioned in between the dipole feed and the length of the coil as shown in Figure 10. The shield was electrically biased to the ground potential of the coil stimulator. The dipole feedlines are on a radial line from the center of the coil, and the dipole wings are oriented on the circumference of circles centered on the coil axis; in this way the dipole should be set up to measure  $-\partial\vec{A}/\partial t$ . The dipole feed position is measured from the center of the coil as the coil is pulsed with 36A peak. A set of dipole feed positions is chosen. At each position a measurement is repeated 64 times and averaged to improve the signal-to-noise ratio.

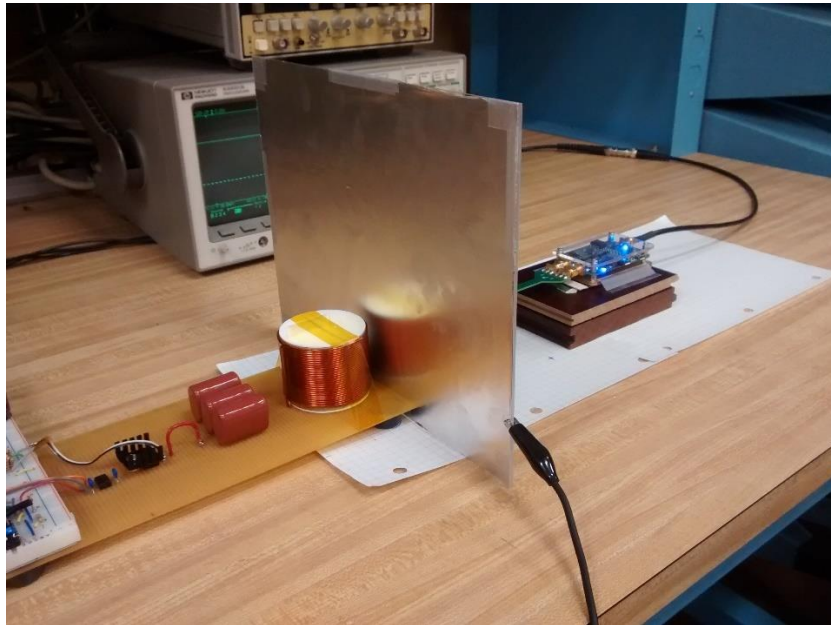


Figure 10: Shield is placed between length of coil and dipole oriented along the circulating magnetic vector potential of the coil

## 4 EXPERIMENTAL RESULTS AND DISCUSSION

In this section the experimental results are presented and discussed. Section 3 discusses the experimental procedures and setup necessary to reproduce the results contained herein. Section 4.1 presents the differential and common-mode frequency responses. Section 4.2 presents the transient step response waveforms. Section 4.3 presents the electric field distributions of the parallel plate capacitor setup. Finally, section 4.4 presents the measured radial fall off of the magnetic vector potential versus distance from the coil axis.

### 4.1 FREQUENCY RESPONSE

This section presents the results for the differential-mode and common-mode frequency domains measurements.

#### 4.1.1 Differential-mode Gain

The normalized differential-mode gain is shown in Figure 11. The 0dB line corresponds to the conversion factor at 3kHz, which is 0.227V of output variation for 1V/cm of incident electric field variation. The phase response around 3kHz is practically 0, demonstrating its suitability for TMS measurements as the pulse waveform is typically a 3kHz bi-stable sinusoidal pulse [21].

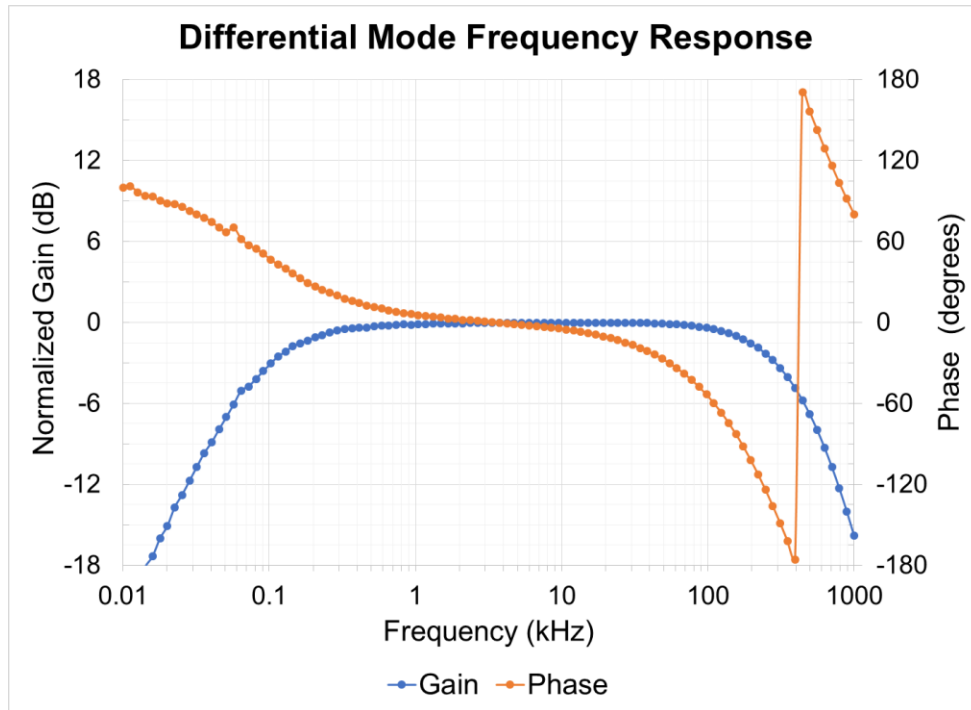


Figure 11: The differential mode conversion factor is normalized to the data point at 3kHz. The conversion factor at 3kHz is 0.227V on the output for 1V/cm of input electric field strength.

### 4.1.2 Common-mode Gain

The common-mode gain is due to a small capacitance that bridges the primary to the secondary side of the HCNR201. That the common-mode gain increases with frequency makes sense owing to the capacitive nature of the parasitic common-mode injection. At 3kHz the probe achieves a common-mode rejection of 50dB as shown in Figure 12. The poorest rejection is at 500kHz with only 16dB of rejection.

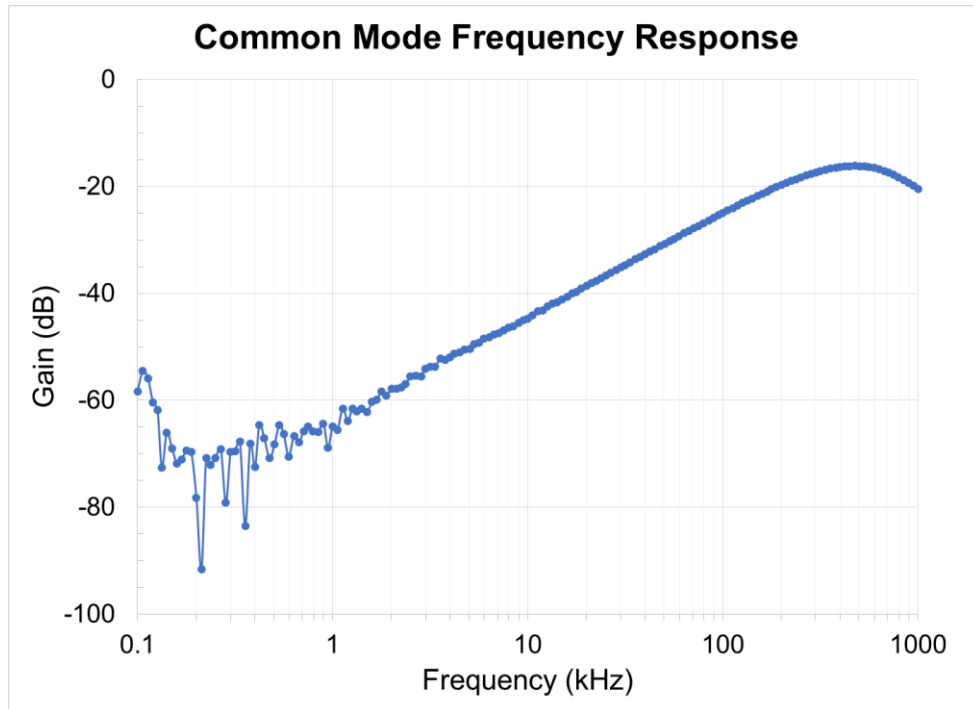


Figure 12.. The common-mode gain is due to the parasitic capacitance bridging the isolation barrier of the HCNR201.

## 4.2 TRANSIENT RESPONSE

Given the frequency response plots of section 4.1, the transient response is expected to have an AC-coupled characteristic at frequencies below 1 kHz as demonstrated in Fig. 13a.

At frequencies greater than 1 kHz, the step response of the probe follows the electric field between the plates with a high fidelity as shown in Fig. 13b. Even at 100 kHz the electric field probe is able to follow the external electric field as shown in Fig. 13c. However, there seems to be an artifact in the output at the onset of the step at 100 kHz. This is due to the common-mode gain of the probe. If the probe orientation is flipped, the artifact appears in the opposite direction. If the isolation is shorted out, this artifact completely disappears as shown in Fig. 13d.

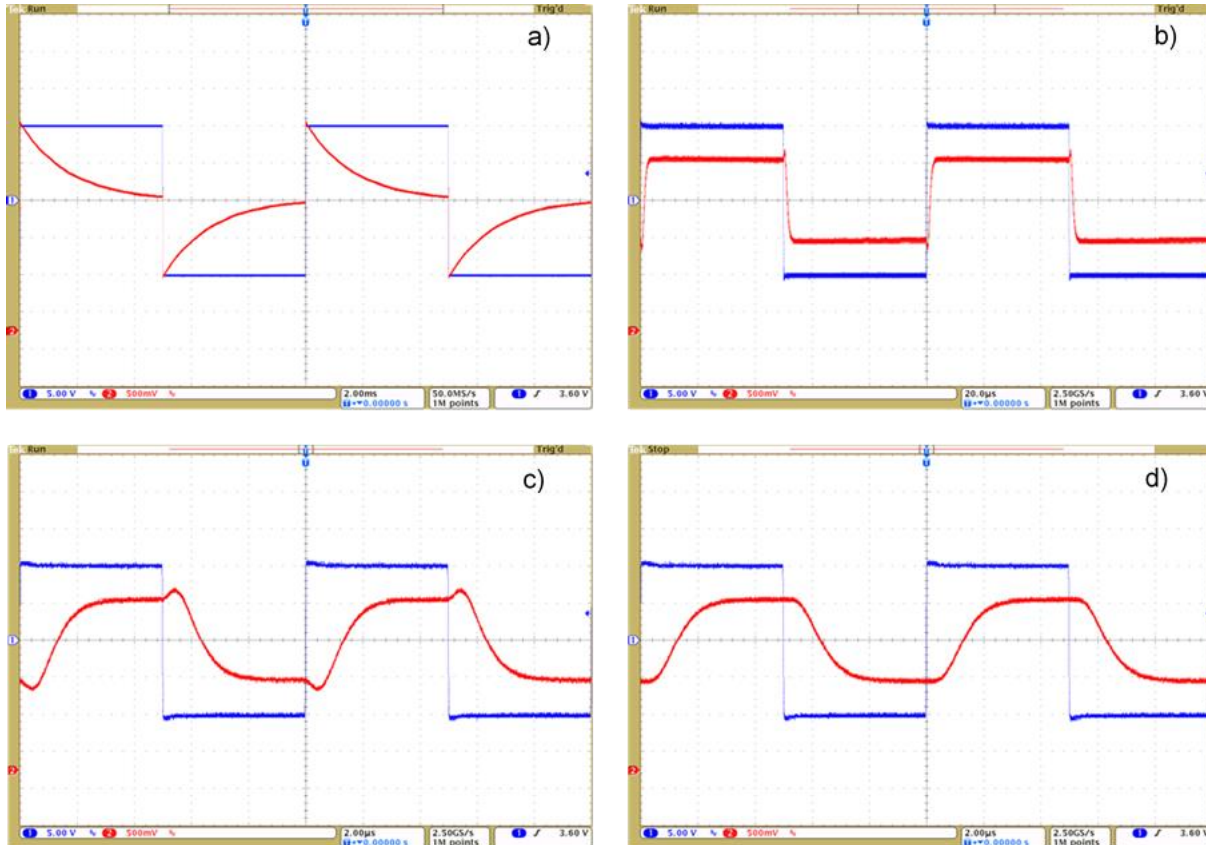


Figure 13. Transient response of the probe. CH1 (blue) is voltage of the driven plate of the parallel plate capacitor. CH2 (red) is the output voltage of the electric field probe. a) –AC-coupled probe output response to a 100 Hz square wave; b) – response to a 10 kHz square wave; c) – response to a 100 kHz square wave with an artifact; d) –the same result as in c) but after shorting the isolation barrier.

### 4.3 QUASISTATIC ELECTRIC FIELD OF PARALLEL PLATE CAPACITOR

The quasi-static electric field pattern was measured along the plane that goes through the center of both circular plates of the cylindrical capacitor described in section 3.3. Figure 13 shows the measured relative electric field magnitude and direction along the half plane from the capacitor center. Note that this plot does not represent a complete data set as I was unable to take x-axis directed field measurements in the region from  $x=0$  to  $x=4$  and  $y=-4$  to  $y=4$ ; it is this reason that the lines are especially straight in that vicinity. MATLAB was used to generate streamline plots of the data in Figure 15. The fringing field lines look convincing qualitatively. However, due to the coarse and incomplete nature of the measured dataset I did not attempt to correlate the measured data with numerical or analytical results. The polarization of the dipole probe was evaluated and confirmed by observing the relative phase of the E-field probe output versus that of the driven plate voltages.

The dominant electric field component was measured between the plates and plotted in Figure 16. Given that the plates were driven by a differential voltage amplitude of 7.6V with a plate separation of 4.128cm, an expected field strength of 1.84V/cm is expected. The only peculiarity noted was an apparent increase in the measured electric field strength as the proximity of the dipole to either plate increased, which is not entirely understood. Tishchenko [38] claims that this effect is due to the wide separation of the plates; the

field would be more constant if the plate separation were reduced or the plate area were increased. This was not experimentally verified. This effect should be investigated in a future work. The performance of the probe in the presence of a quasi-static electric field within the capacitor was found satisfactory.

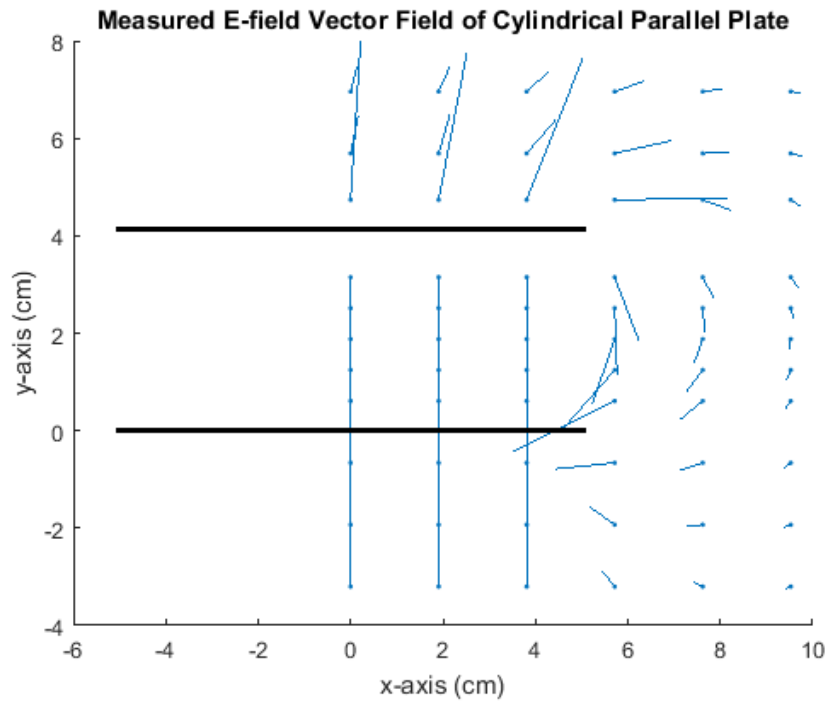


Figure 14. Vector field plot of electric field. Only  $x$ -hat components of the E-field were measured in the region from  $x=0$  to  $x=4$  and  $y=-4$  to  $y=4$

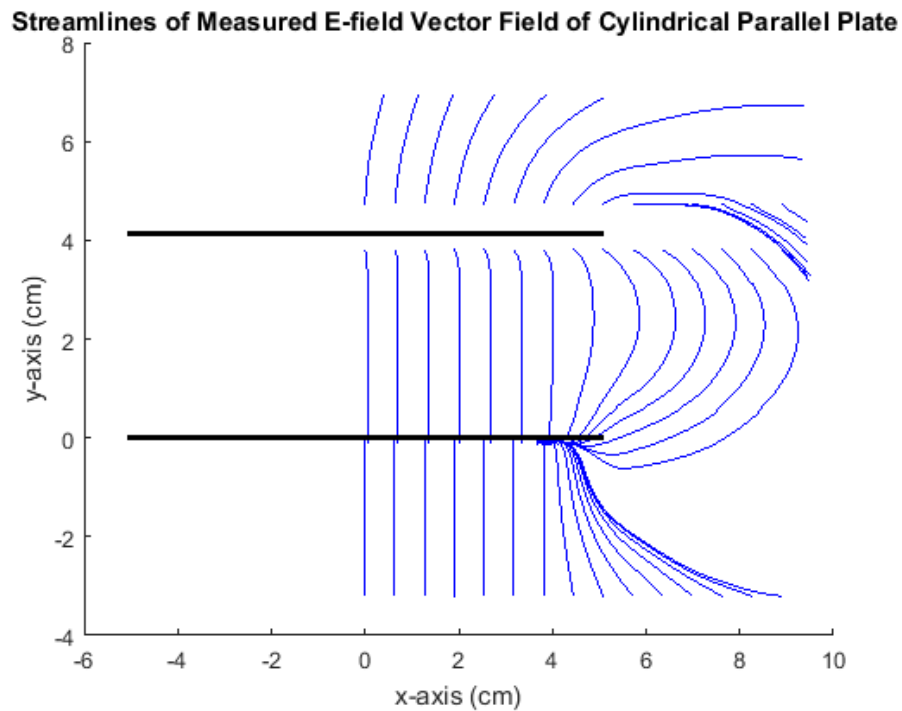


Figure 15: Streamlines of the E-field vector field shown in Figure 14.

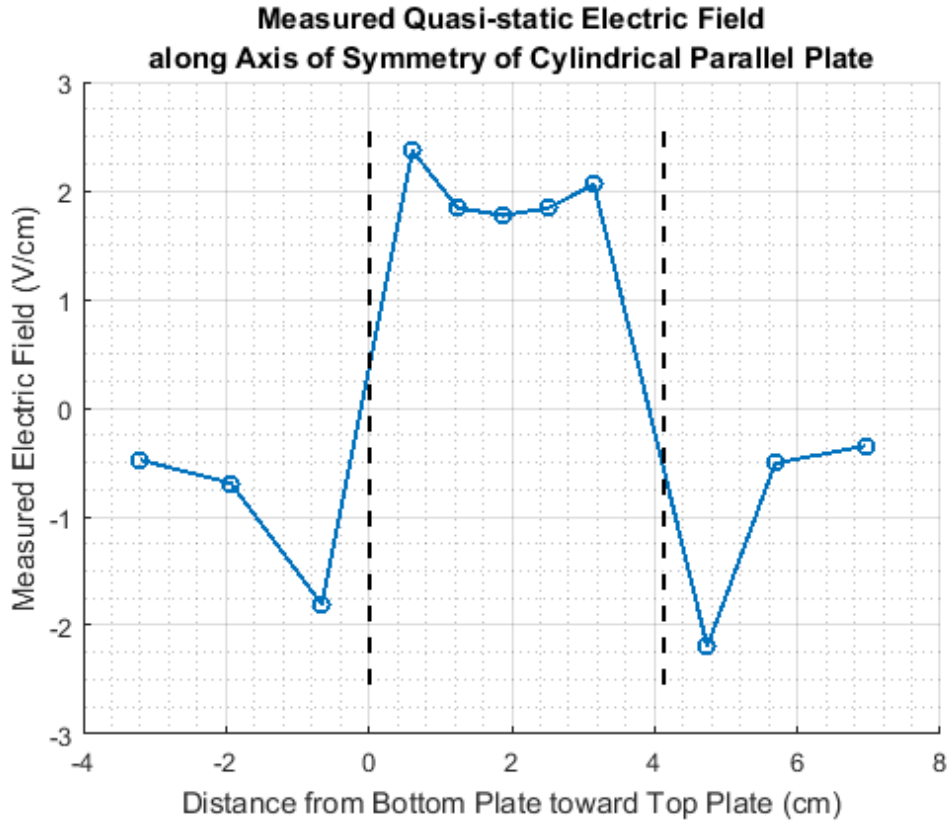


Figure 16. Dominant electric-field component inside and outside the parallel-plate capacitor setup described in section 4.3. The dotted lines represent the capacitor plates. The capacitors were driven by a differential voltage amplitude of 7.6V, corresponding to an expected field strength of 1.84V/cm between the plates.

#### 4.4 QUASISTATIC ELECTRIC FIELD OF SOLENOID

The magnetic vector potential,  $\vec{A}$ , of a solenoid forms a circulating vector field pattern centered at the coil axis. The induced electric field pattern, or  $\vec{E} = -\partial\vec{A}/\partial t$ , should follow this pattern. For a sinusoidal current pulse, the expected induced field waveform would therefore be a cosine pulse.

There are two critical details that need to be accounted for to accurately complete this measurement. The first item is that an electrostatic shield is absolutely necessary to block any fields due to charge (i.e.  $-\nabla\phi$ ) that are generated in the process of pulsing the coil. In fact, Glover [12] explicitly claims that the bioelectrode-based dipole probe is not useful in air since its measurements are dominated by electrostatic fields. For a demonstration of this fact consider the waveforms shown in Figure 17. The coil setup of section 3.4 was altered to align the dipole wings along the length of the coil where there is naturally no  $-\partial\vec{A}/\partial t$ . The left waveform in Figure 17 measures the probe output voltage when there is no shield between the dipole and the coil. The right waveform measures the probe output voltage when the shield is inserted. Only with the shield am I able to measure the correct  $-\partial\vec{A}/\partial t$ .

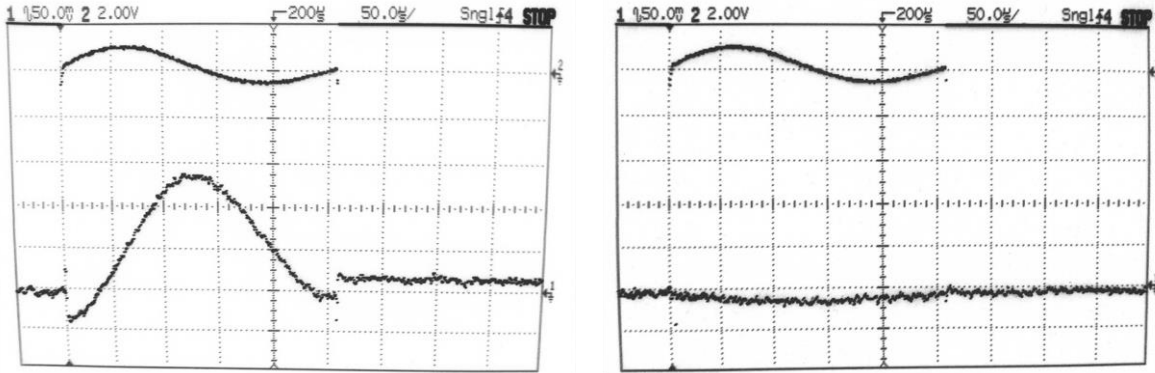


Figure 17: The coil setup of section 3.4 was altered to align the dipole wings along the length of the coil where there is naturally no  $-\partial A/\partial t$ . The left waveform in Figure 17 measures the probe output voltage when there is no shield between the dipole and the coil. The right waveform measures the probe output voltage when the shield is inserted.

The second issue alluded to in section 2.1 was the presence of the parasitic  $\partial \vec{B}/\partial t$  at the SMA connector bridge. This was a pernicious little hardware bug that only showed up when I got around to reducing the measurement data. As shown in Figure 18 the measured E-field probe output voltage was significantly greater than expected probe output voltage due to  $-\partial \vec{A}/\partial t$  at the probe tip. The expected  $-\partial \vec{A}/\partial t$  was numerically evaluated in Excel using the closed form expressions in terms of elliptical integrals that was given on Wikipedia [39].

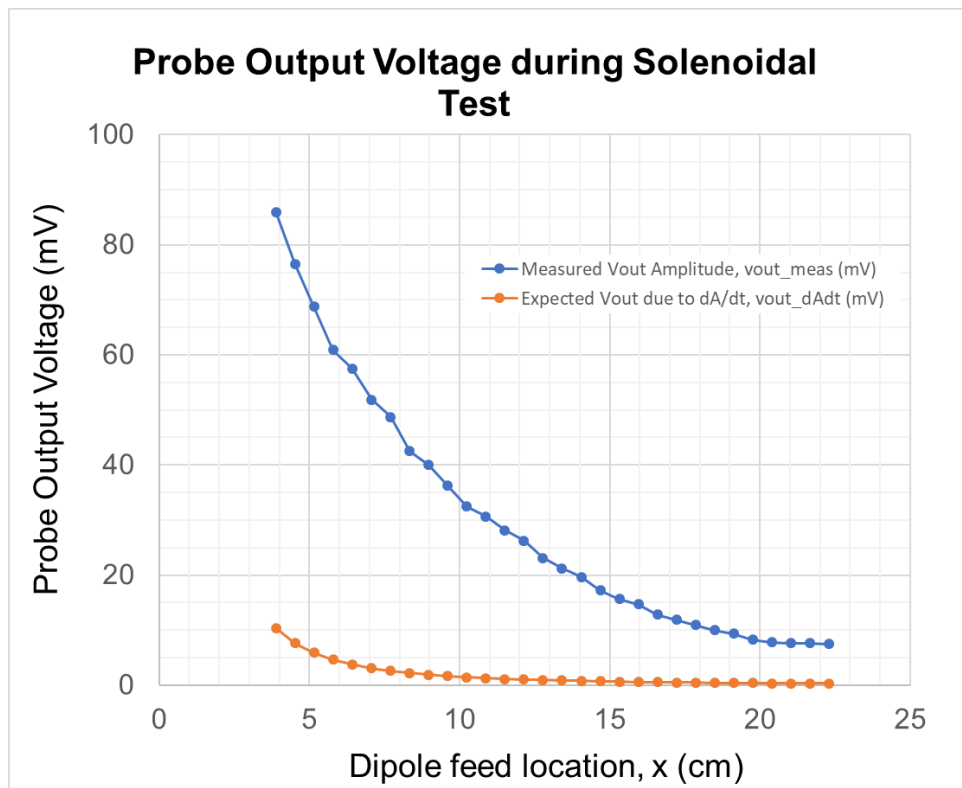


Figure 18: Initial data reduction comparing measured data to expected data for the solenoidal field tests

This prompted me to take a second look at the layout and construction of the probe. It is then that I noticed the parasitic  $\partial \vec{B}/\partial t$  made by the SMA connector bridge between the dipole/balun PCB and the

instrumentation PCB as shown in Figure 19. I then proceed to re-evaluate the Excel model based on [39]. After including the *emf* of this parasitic loop the measured data began to make sense as shown in Figure 20. This contribution is calculated by computing the capacitive voltage divider formed between  $C_{in}$  and  $(C_{tot} - C_{in})$  as defined in section 2.3; call this capacitive divider gain  $k_v$ . The *emf* around the loop was calculated by taking the  $\partial \vec{B} / \partial t$  normal to the center of the parasitic loop and multiplying it by the loop area to get the change in flux. If the amplifier gain from the instrumentation input to the probe output is denoted by  $A_v$ , the probe output voltage due to the parasitic SMA connector bridge loop is simply the  $emf * k_v * A_v$

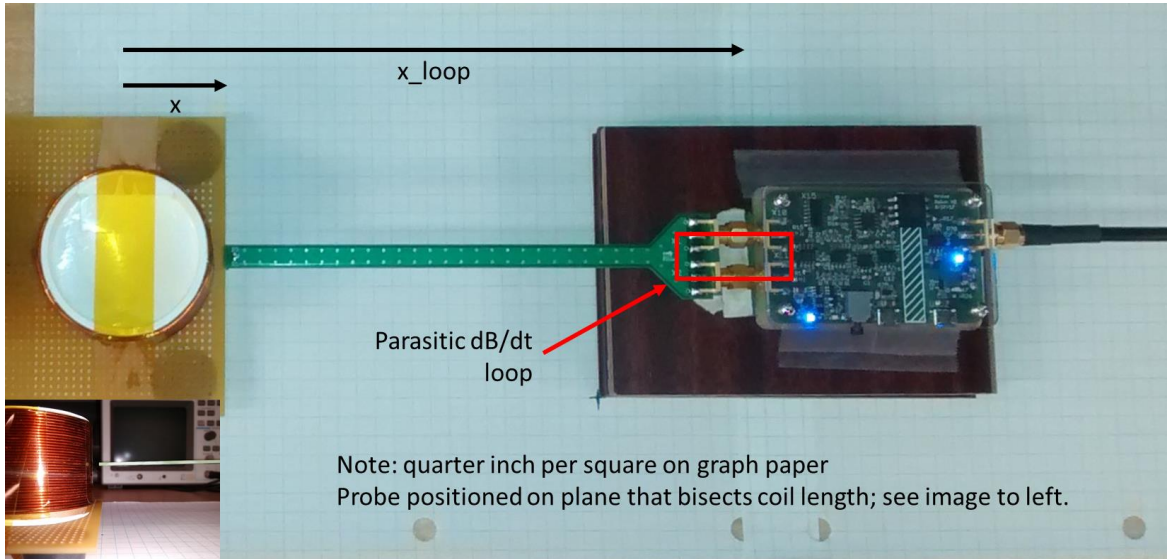


Figure 19: Illustration showing parasitic dB/dt loop made by SMA connector bridge.

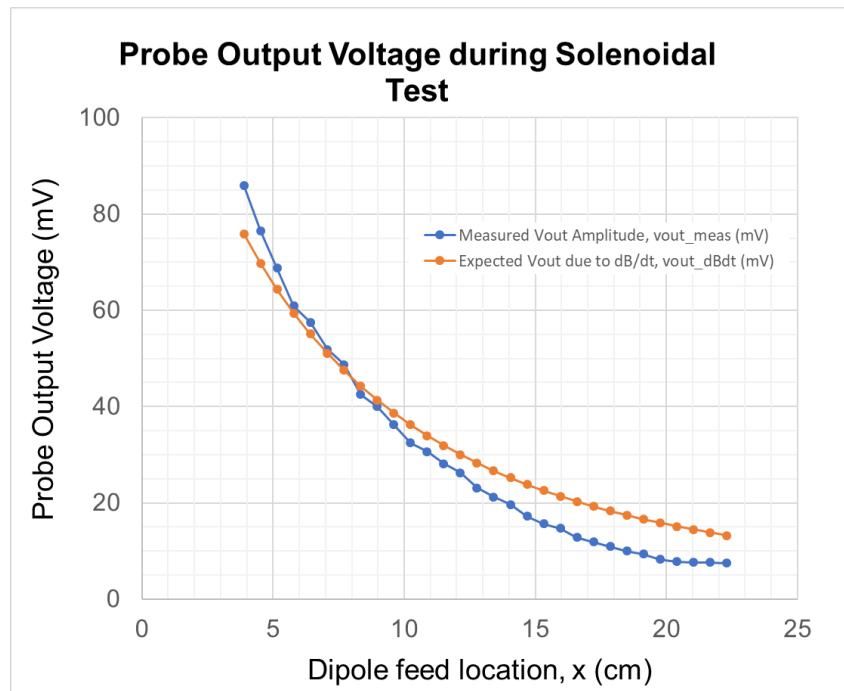


Figure 20: Expected Probe output when only the contribution from the dB/dt loop is include.

Once the loop was eliminated by cutting and re-routing the feedline as shown in Figure 5 the measured

$-\partial\vec{A}/\partial t$  agreed much more closely with the expected result given by numerical evaluation of the expected solenoidal field [39] as shown in Figure 21. The remaining difference between the measured and computed data is possibly due to stray magnetic field linking a small but finite gap between the feedlines.

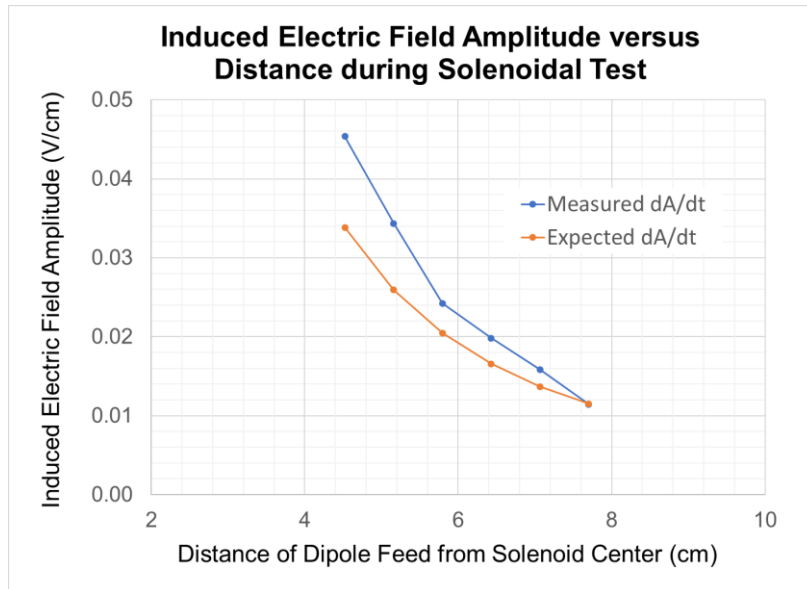


Figure 21. The measured  $dA/dt$  versus the expected  $dA/dt$  as evaluated by the expression in [39]

Finally, a waveform of the induced waveform is shown in Figure 22. Notice that the probe's output voltage is a cosine pulse given a sine pulse current through the coil.



Figure 22: Measured induced electric field waveform at  $x=4.524\text{cm}$ ; the SNR at these measurement amplitudes was improved by averaging the waveform 64 times resulting in the waveform shown. CH1 (blue) is the coil current measured with a separate current probe in series with the coil, and CH2 (red) is the output voltage of the electric-field probe. The excitation frequency is 3.846kHz.

## 5 CONCLUSION AND FUTURE WORK

---

I began this paper by making the case for the need for empirical tools in the evaluation of primary and secondary fields in volume conductors under TMS stimulation. I then reviewed past research pursued for this purpose and compared the relative advantages and disadvantages of each prior approach. I then proposed the electrically small dipole with a capacitive load and reviewed in detail its implementation and characterization results. Lastly, I demonstrated my E-field probe's ability to measure electric field due to charges alone, or secondary fields in the case of TMS, along with my probe's ability to measure induced electric fields due to currents alone, or primary fields in the case of TMS.

Given all of the results that have been presented so far, the last questions I will tackle here are the following:

- 1) How does this probe compare with the others?
- 2) How can it be improved?

As designed this probe was demonstrated to be able to individually measure both components of the complete electric field in Eq. 2. The only nuisance was that an electrostatic shield was required for the solenoidal field measurements. This shield should not be necessary if the probe is immersed in tissue or a saline solution as the medium should be able to provide the shielding. With this insight the probe should be able to measure the complete electric field in a volume conductor just like the bioelectrode-based probes discussed previously.

Unlike the bioelectrode-based E-field probes, which should ideally be designed to have a stable voltage gain of unity over time and temperature when immersed in the prerequisite electrolytic solution, the voltage gain of the capacitively coupled dipole antenna will always be a function of the permittivity of the surrounding medium, owing to the fact that the antenna capacitance is a function the surrounding permittivity. This means that as constructed the gain of this work's probe will vary and drift when immersed in an electrolytic bath.

With some ingenuity one way this problem could be resolved is by using an automatic gain control (AGC) circuit. A circuit could be designed to inject a known signal, say a differential current impulse across the antenna feedlines, and measure the voltage response at the output of the first gain stage. With a known stimulus and a measured response, it is possible to determine the antenna capacitance in principle. With the antenna capacitance known the circuit could automatically adjust the system gain, which would make the probe tolerant to changes in permittivity in different media and most importantly a time-variant permittivity like that of an electrolytic bath.

With this point made it seems that the capacitively loaded small dipole antenna of this work could be made to work in an electrolytic solution just like the standard bioelectrode-based electric field probes of section 1.1.1. However, I would like to make the point that the bioelectrode-based dipole cannot be easily made to work in air, owing to the very wide impedance swing that occurs as the bio-electrodes exit the electrolytic test medium. As an example, consider the bioelectrode-based dipole that Salanas created for his research in [19]. Salanas explains that the only necessary instrumentation for his dipole is an oscilloscope. In other words, he is able to make measurements to within an accuracy of 2.6V/m, which is very comparable to that of this work, by simply connecting the dipole feedlines to two channels of an oscilloscope. Outside of the electrolytic solution his dipole is in principle no different from this work's dipole; in other words, it will lose the benefit of the low impedance afforded by the charge-transfer resistance,  $R_{CT}$ , and the double-

layer capacitance,  $C_{DL}$ . As such the transduced signal will be miniscule as demonstrated by this work, where a gain of 300V/V and careful tuning of the input filter network was required to sufficiently amplify the signal at a reasonable SNR.

Being able to measure electric fields in air is a big advantage. In his paper Niemenin [21] demonstrated an automated, robotized system able to readily sweep the electric field in air, which is something that would be rather difficult to do in an electrolytic medium. In principle the probe of this work could be used to do the same thing with the prerequisite shield to block the electrostatic field. In this way the utility of this work's probe can be seen to be somewhere in between that of Niemenin's triangular loop and Epstein/Salanas long rectangular loop. Both the rectangular probe and this work's probe can only measure the primary electric field component in air, but this work's probe can in general do it with a single measurement. Just like this work's probe the triangular loop also only needs a single measurement, but it has the additional benefit of being a phantom measurement for the electric field of a spherical volume conductor, which is truly remarkable, and puts it in a class of its own.

At present what prevents our probe from being used in its capacity to measure primary electric fields in air as described in the last paragraph is the lack of a high quality electrostatic shield that produces negligible secondary fields. The shield developed in this work was done so merely as a proof of concept not as a serious attempt.

## 6 BIBLIOGRAPHY

---

- [1] M. Hallet, "Transcranial Magnetic Stimulation: A Primer," *Neuron*, vol. 55, no. 2, pp. 187-199, 2007.
- [2] A. T. Barker, R. Jalinous and F. I. L., "Non-invasive magnetic stimulation of human motor cortex," *Lancet*, vol. 1, no. 8437, pp. 1106-1107, 1985.
- [3] A. Nummenmaa, M. Stenroos, R. Ilmoniemi, Y. Okada, M. Hämäläinen and T. Raij, "Comparison of spherical and realistically shaped boundary element head models for transcranial magnetic stimulation navigation," *Clinical Neurophysiology*, vol. 124, no. 2013, pp. 1995-2007, 2013.
- [4] S. N. Makarov, G. M. Noetscher and A. Nazarian, "Fundamentals of Eddy Currents," in *Low Frequency Electromagnetic Modeling for Electrical and Biological Systems using MATLAB*, Hoboken, N. J., John Wiley & Sons, Inc., 2016, pp. 425-470.
- [5] N. M. Branston and P. S. Tofts, "Analysis of the distribution of currents induced by a changing magnetic field in a volume conductor," *Physics in Medicine and Biology*, vol. 36, no. 2, pp. 161-168, 1991.
- [6] E. McAdams, "Bioelectrodes," in *Encyclopedia of Medical Devices and Instrumentation*, J. G. Webster, Ed., Hoboken, New Jersey: Wiley-Interscience, 2006, pp. 120-166.
- [7] J. O. Bockris and S. U. M. Khan, "The Interphasial Structure," in *Surface Electrochemistry: A Molecular Level Approach*, New York, Springer Science+Business, 1993, pp. 59-166.
- [8] T. J. Swiontek, A. Sances, S. J. Larson, J. J. Ackmann, J. F. Cusick, G. A. Meyer and E. A. Millar, "Spinal Cord Implant Studies," *IEEE Transactions on Biomedical Engineering*, vol. 23, no. 4, pp. 307-312, 1976.
- [9] G. Tay, M. Chilbert, J. Battocletti, A. Sances, Swiontek and C. T. Kurakami, "Measurement of Magnetically Induced Current Density in Slaine and in vivo," in *IEEE Engineering in Medicine and Biology Society 11th Annual International Conference*, 1989.
- [10] G. Tay, M. Chilbert, J. Battocletii, A. Sances and T. Swiontek, "Mapping of current densities induced in vivo during magnetic stimulation," in *Annual International Conference of the IEEE Engineering in Medicine and Biology Society*, 1991.
- [11] S. Deutsch, "A Probe to Monitor Electroanesthesia Current Density," *IEEE Transactions on Biomedical Engineering*, vol. 15, no. 2, pp. 130-131, 1968.
- [12] P. M. Glover and R. Bowtell, "Measurement of electric fields due to time-varying magnetic field gradients using dipole probes," *Physics in Medicine and Biology*, vol. 52, no. 17, pp. 5119-5130, 2007.

- [13] D. Durand, A. S. Ferguson and T. Dalbasti, "Induced electric fields by magnetic stimulation in non-homogenous conducting media," in *Proceedings of the Annual International Engineering in Medicine and Biology Society*, Seattle, WA, 1989.
- [14] P. S. Tofts and N. M. Branston, "The measurement of electric field, and the influence of surface charge, in magnetic stimulation," *Electroencephalography and Clinical Neurophysiology*, vol. 81, no. 3, p. 238, 1991.
- [15] F. X. Hart and K. W. Wood, "Eddy current distributions: Their calculation with a spreadsheet and their measurement with a dual dipole antenna probe," *American Journal of Physics*, vol. 59, no. 5, pp. 461-467, 1991.
- [16] P. J. Maccabe and e. al, "Magnetic coil stimulation of straight and bent amphibian and mammalian peripheral nerve in vitro: locus of excitation," *The Journal of Physiology*, vol. 460, no. 1, pp. 201-219, 1993.
- [17] P. Mirtaheri, S. Grimnes and G. Martinsen, "Electrode polarization impedance in weak NaCl aqueous solutions," *IEEE transactions on Biomedical Engineering*, vol. 52, no. 12, pp. 2093-2099, 2005.
- [18] C. M. Epstein and e. all, "Localizing the site of magnetic brain stimulation in humans," *Neurology*, vol. 40, no. 4, p. 666, 1990.
- [19] F. S. Salinas, J. L. Lancaster and P. T. Fox, "3D modeling of the total electric field induced by transcranial magnetic stimulation using the boundary element method," *Physics in Medicine and Biology*, vol. 54, no. 12, p. 3631, 2009.
- [20] F. S. Salinas, J. L. Lancaster and P. T. Fox, "Detailed 3D Models of the induced electric field of transcranial magnetic stimulation coils," *Physics in Medicine and Biology*, vol. 52, no. 10, pp. 2879-2892, 2007.
- [21] J. O. Nieminen, L. M. Koponen and R. J. Ilmoniemi, "Experimental Characterization of the Electric Field Distribution Induced by TMS Devices," *Brain Stimulation*, vol. 8, no. 3, pp. 582-589, 2015.
- [22] R. J. Ilmoniemi, M. S. Hämäläinen and J. Knuutila, "The forward and inverse problems in the spherical model," in *Biomagnetism: Applications & Theory*, H. Weinberg, G. Stroink and T. Katila, Eds., New York, Pergamon Press, 1985, pp. 278-282.
- [23] R. J. Ilmoniemi, "The triangle phantom in magnetoencephalography," *Journal of Japan Biomagnetism and Bioelectromagnetics Society*, vol. 22, no. 1, pp. 44-45, 2009.
- [24] D. Cohen, "The MEG made ridiculously simple," 2009. [Online]. Available: [http://www.nmr.mgh.harvard.edu/meg/pdfs/talks/Cleve\\_Cohen\\_WithNotes2g.pdf](http://www.nmr.mgh.harvard.edu/meg/pdfs/talks/Cleve_Cohen_WithNotes2g.pdf). [Accessed 15 March 2018].

- [25] M. Kanda, "Standard probes for electromagnetic field measurements," *IEEE Transactions on Antennas and Propagation*, vol. 41, no. 10, pp. 1349-1364, 1993.
- [26] G. S. Smith, "Limitations on the size of miniature electric-field probes," *IEEE Transactions on Microwave Theory and Techniques*, vol. 32, no. 6, pp. 594-600, 1984.
- [27] S. Ohoka, F. Asakura and H. Taki, "Electric field probe using a differential amplifier circuit with high input impedance," *Asia-Pacific Symposium on Electromagnetic Compatibility*, pp. 554-556, 2015.
- [28] B. Yang, W. Zhang, X. Cui and J. Chen, "Research of electric-field strength measurement based on a top-loaded antenna in the near field," *Asia-Pacific Symposium on Electromagnetic Compatibility and 19th International Zurich Symposium on Electromagnetic Compatibility*, pp. 602-605, 2008.
- [29] S. Kuehn, S. Pfeifer, B. Kochali, E. Grobbelaar, P. Sepan and N. Kuster, "A Novel Automated Phasor Measurement System for Validated and Traceable EMC/EMI Near-Field Analysis," *IEEE Electromagnetic Compatibility Magazine*, vol. 5, no. Q2, pp. 41-46, 2016.
- [30] H. Bassen and G. Smith, "Electric field probes-A review," *IEEE Transactions on Antennas and Propagation*, vol. 31, no. 5, pp. 710-718, 1983.
- [31] P. Jarrige, N. Ticaud, S. Kohler, R. P. O'Conner, L. Duvillaret, G. Gaborit, D. Arnaud-Cormos and P. Leveque, "Electrooptic Probe Adapted for Bioelectromagnetic Experimental Investigations," *IEEE Transactions on Instrumentation and Measurement*, vol. 61, no. 7, pp. 2051-2058, 2012.
- [32] S. Wakana and e. al, "Fiber-edge electrooptic/magneto optic probe for spectral-domain analysis of electromagnetic field," *IEEE Transactions on Microwave Theory and Techniques*, vol. 48, no. 12, pp. 2611-2616, 2000.
- [33] M. Bernier, G. Gaborit, L. Duvillaret, A. Paupert and J. L. Lasserre, "Electric field and temperature measurement using ultra wide bandwidth pigtailed electro-optic probes," *Applied Optics, Optical Society of America*, vol. 47, no. 13, pp. 2470-2476, 2008.
- [34] T. Zhu, L. Zhou, M. Liu, J. Zhang and L. Shi, "High sensitive space electric field sensing based on micro fiber interferometer with field force drive gold nanofilm," *Nature Scientific Reports*, 2015.
- [35] J. C. Mosher, "A Review on the Importance of Volume Currents," in *14th International Conference on Biomagnetism*, Boston, MA, 2004.
- [36] J. D. Dyson, "Measurement of near fields of antennas and scatterers," *IEEE Transactions on Antennas and Propagation*, vol. 21, no. 4, pp. 446-460, 1973.
- [37] J. D. Dyson and R. Ginyovsky, "Balanced Transmission-Line Measurements Using Coaxial Equipment (Correspondence)," *IEEE Transactions on Microwave Theory and Techniques*, vol. 19, no. 1, pp. 94-96, 1971.

- [38] V. A. Tishchenko, V. I. Tokatly and V. I. Lukyanov, "Calculation of the field of a parallel-plate capacitor for calibrating electric field strength converters with a grounded plate," *Measurement Techniques*, vol. 55, no. 4, pp. 459-462, 2012.
- [39] "Wikipedia - Solenoid: Finite continuous solenoid," [Online]. Available: [https://en.wikipedia.org/wiki/Solenoid#Finite\\_continuous\\_solenoid](https://en.wikipedia.org/wiki/Solenoid#Finite_continuous_solenoid). [Accessed 15 March 2018].
- [40] K. Yunokuchi and D. Cohen, "Developing a more focal magnetic stimulator. Part II: Fabricating coils and measuring induced current distributions," *Journal of Clinical Neurophysiology*, vol. 8, no. 1, p. 112, 1991.
- [41] T. Wagner and e. al, "Intracranial measurement of current densities induced by transcranial magnetic stimulation in the human brain," *Neuroscience Letters*, vol. 354, no. 2, pp. 91-94, 2004.
- [42] E. E. Aslan, "Electromagnetic Radiation Survey Meter," *IEEE Transactions on Instrumentation and Measurement*, vol. 19, no. 4, pp. 368-372, 1970.
- [43] E. E. Aslan, "Broad-band Isotropic Electromagnetic Radiation Monitor," *IEEE Transactions on Instrumentation and Measurement*, vol. 21, no. 4, pp. 421-424, 1972.
- [44] Z. Deng, S. H. Lisanby and A. V. Peterchev, "Electric field depth-focality tradeoff in transcranial magnetic stimulation: Simulation comparison of 50 coil designs.," *Brain Stimulation*, vol. 6, no. 1, pp. 1-13, 2013.
- [45] P. M. Glover and R. Bowtell, "Measurement of electric fields induced in a human subject due to natural movements in static magnetic fields or exposure to alternating magnetic field gradients," *Physics in Medicine and Biology*, vol. 53, no. 2, pp. 361-373, 2008.
- [46] J. R. Melcher and D. Cohen, "Dependence of the MEG on dipole orientation in the rabbit head," *Electroencephalography and clinical Neurophysiology*, vol. 70, no. 5, pp. 460-472, 1988.
- [47] P. A. Merton and H. B. Morton, "Stimulation of the cerebral cortex in the intact human subject," *Nature*, vol. 285, p. 227, 1980.

## 7 APPENDIX A: ANCILLARY CIRCUITRY ON INSTRUMENTATION PCB

Figure 23 shows the block diagram for the system implemented on the instrumentation PCB. Figure 24 shows how the various blocks are distributed on the PCB. Both the floating and grounded circuits are powered off of a 3.7V Lithium-ion polymer battery. These batteries were sized for 400mAh each. The majority of the quiescent current consumed by the instrument is on the floating side, owing to the large number of opamps and the 4mA required bias current in the LED for the HCNR201. As such a little push-button state-machine was implemented using a ripple counter to enable the user to turn off the device as shown in Figure 25. If a simple power button were desired a simple switch could have been used; however, I also wanted to implement a test-mode that switches in the high pass filter whose frequency response is plotted of Figure 26. This was intended to help in the debugging of anticipated 60Hz hum.

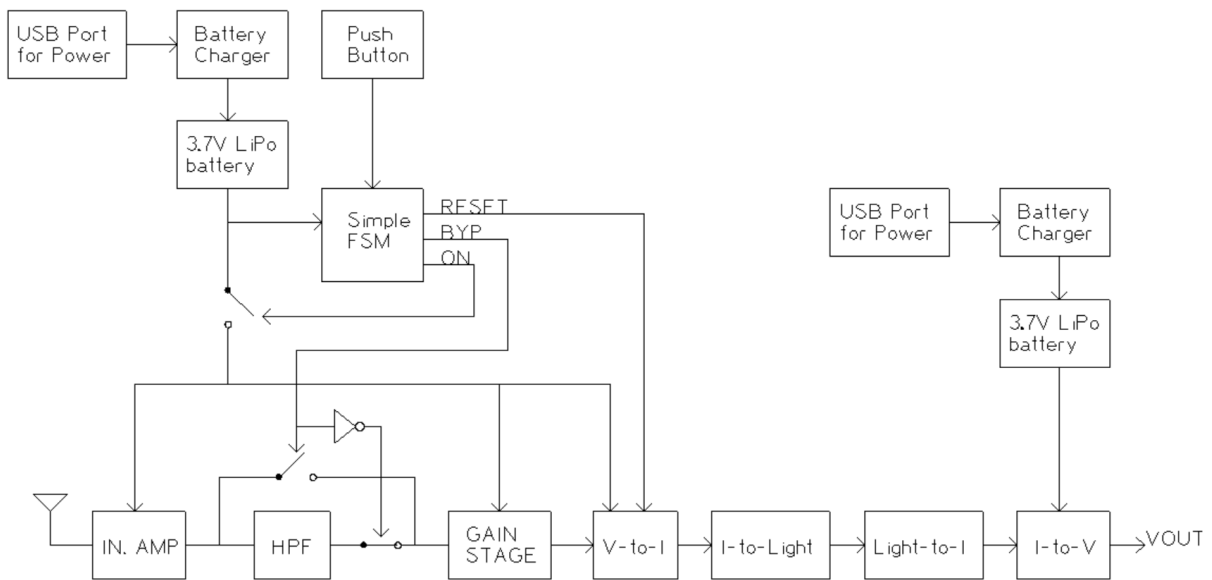


Figure 23. Block diagram showing battery power and push-button state machine

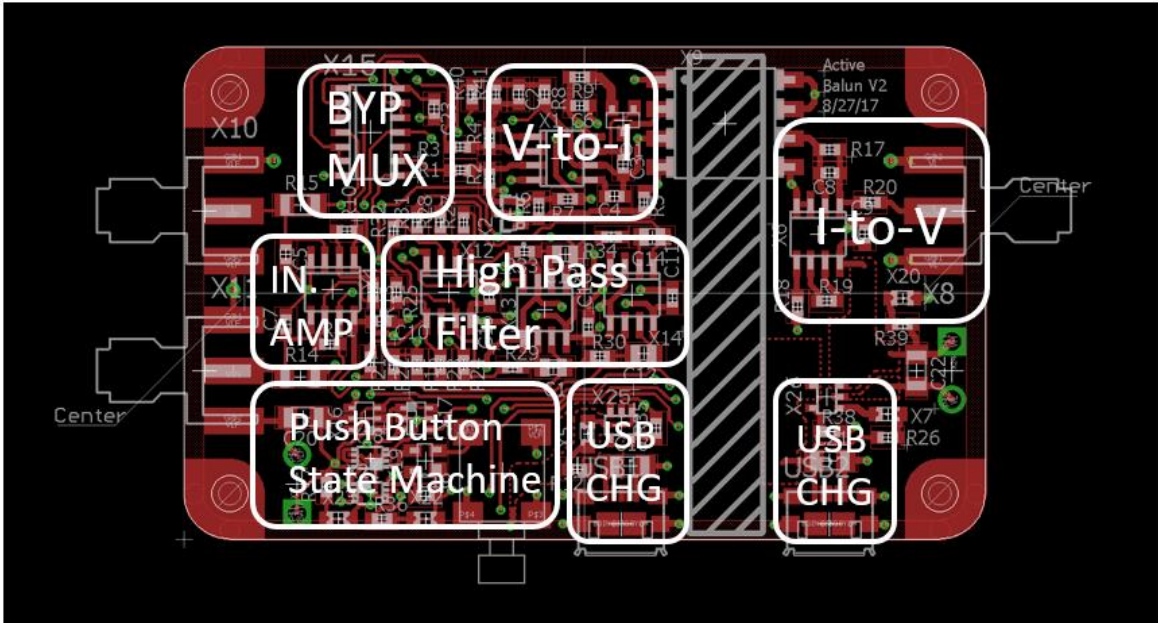


Figure 24. Placement of blocks shown in Fig. 23.

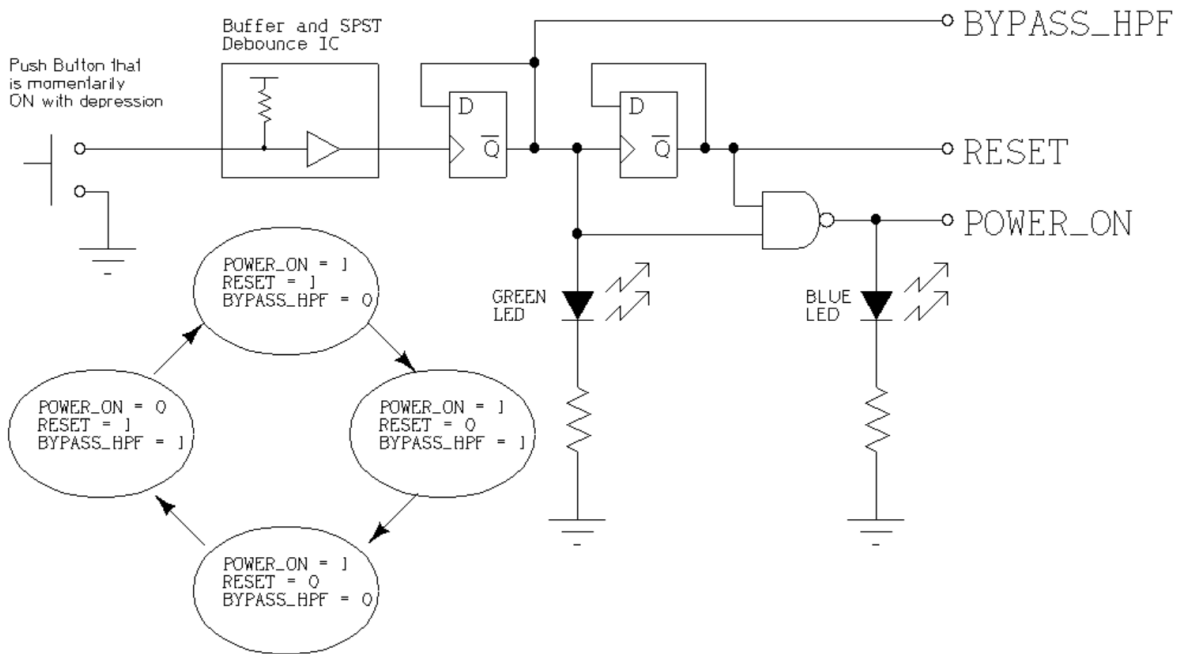


Figure 25. Simple FSM for high-pass filter (HPF) bypass and ON/RESET control

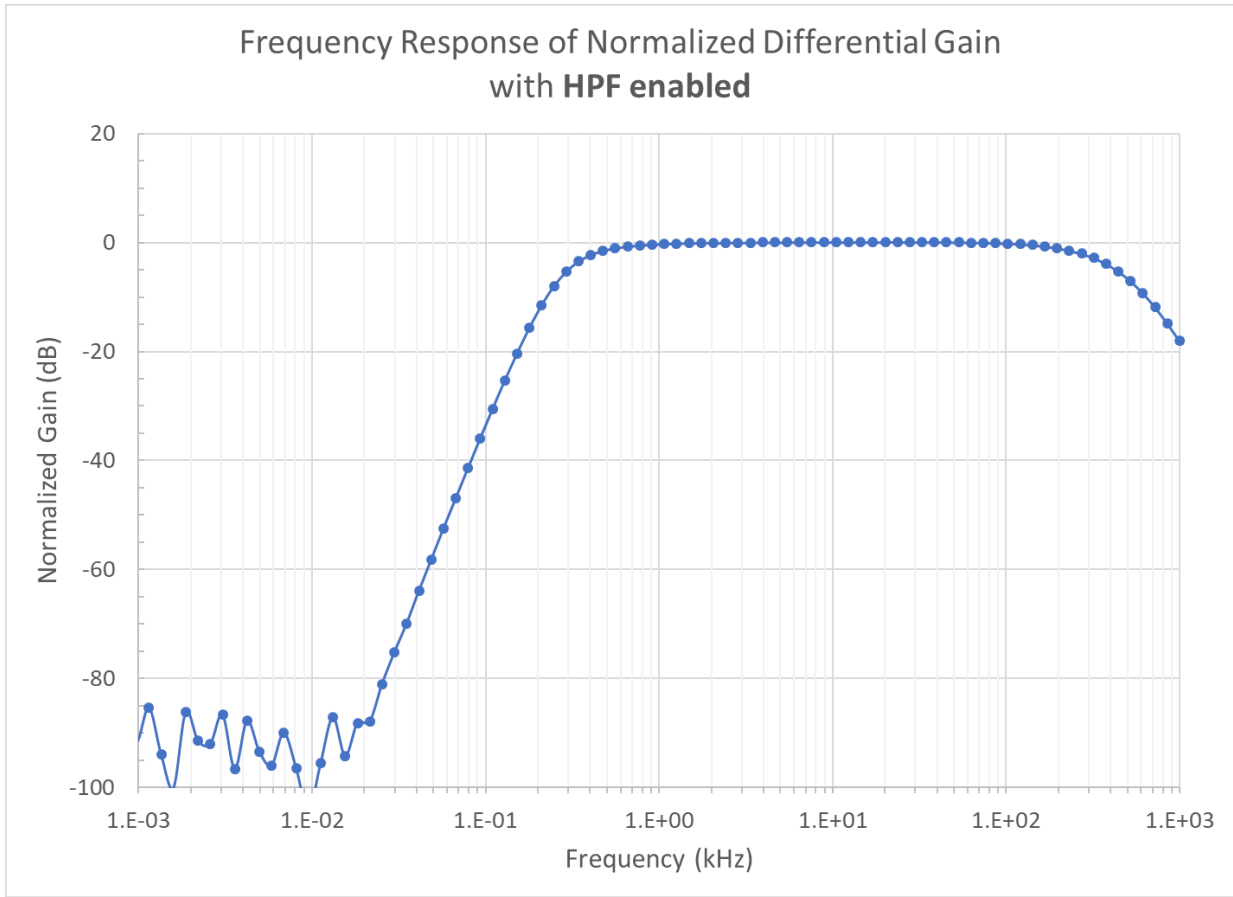


Figure 26. This plot shows the measured differential mode gain response with the high-pass filter enabled. The high-pass filter was implemented as a 4<sup>th</sup> order Bessel filter with corner frequency at 360Hz, providing 50dB of attenuation at 60Hz. The data was normalized to the conversion gain at 3kHz, which measured to be 0.227V of output voltage for 1V/cm of incident electric field. The inclusion of this filter was intended as a test-mode.

## 8 APPENDIX B: SOFT-SWITCHED MOSFET-BASED STIMULATOR

An experimental setup for measuring the induced electric field of a solenoidal coil is much more involved than the test setup for measuring the quasi-static electric field of the parallel-plate capacitor of Section 3.3. The major difficulty of the new setup is in pulsing the coil with a sufficiently high enough current to produce reasonable electric-field levels for measurement. Therefore, we will describe our test setup in detail.

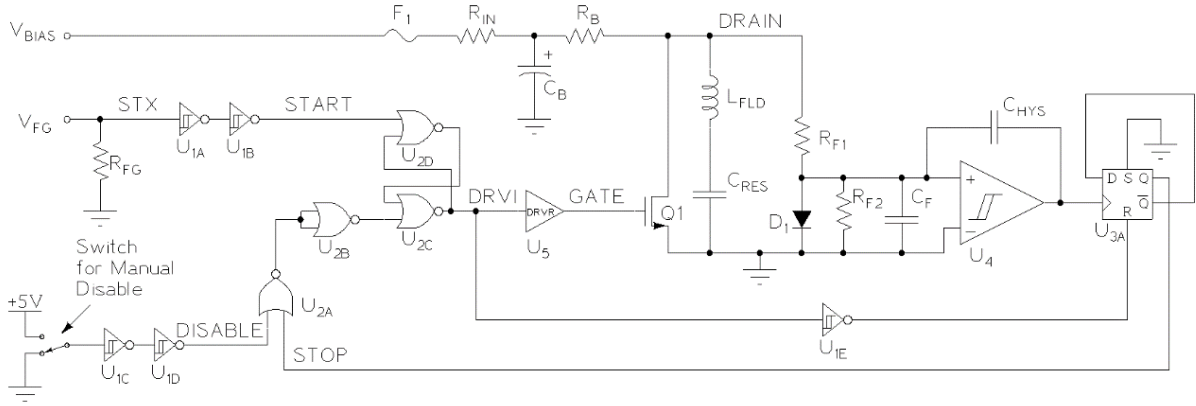


Figure 27. Schematic for a bi-stable current pulse generator for induced E-field measurements with a solenoid. Decoupling/bypass capacitors and unused circuits (in multi-circuit parts) are not shown.

The schematic for the solenoidal test system is shown in Fig 27. This circuit applies a single-shot sinusoidal current pulse to the coil via a series resonant RLC circuit made by the coil inductance  $L_{FLD}$ , the resonant capacitance  $C_{RES}$ , and the total series resistance from the MOSFET  $Q_1$  and the equivalent series resistances of reactive components and interconnecting wires. The pulse current amplitude, neglecting damping, is equal to the initial voltage of  $C_{RES}$  divided by the tank impedance, e.g.  $\sqrt{L_{FLD}/C_{RES}}$ ; and the pulse frequency is equal to  $(2\pi\sqrt{L_{FLD}C_{RES}})^{-1}$ .

To operate the test setup, a bias voltage is applied to the  $V_{BIAS}$  port. The current pulse is initiated by pulsing the  $V_{FG}$  with a manually triggered 1 $\mu$ s, 5V single-shot pulse using a pulse generator. To first order the resultant peak current pulse amplitude is given by

$$i_{coil} \approx \frac{R_{F1}}{(R_{F1} + R_B)} \frac{V_{BIAS}}{\sqrt{L_{FLD}/C_{RES}}}$$

The largest bias voltage utilized in testing was 60 V, resulting in peak coil current of 36 A. Since significant reactive power is processed in the operation of this circuit it is critical to reliably turn off the switch at the end of the bi-stable pulse. For this reason, the test setup implements a zero-crossing detector to automatically soft-switch  $Q_1$  off.

The component values used in our implementation are the following:  $R_{FG}=50 \Omega$ ,  $U_1$ =Texas Instruments CD40106B,  $U_2$ =Texas Instruments CD4001UB,  $U_3$ = Texas Instruments CD4013B,  $U_4$ =Advanced Linear

Devices ALD2302,  $U_5$ =Texas Instruments UCC27322,  $Q_1$ =International Rectifier IRL2910PBF,  $D_1 = 1N4148$ ,  $R_{IN}=10 \Omega$ ,  $F_1=250V/500mA$  fuse,  $C_B= 33\mu F$ , 100V, aluminum electrolytic with  $\sim 1\text{ohm}$  ESR,  $R_B=200 \Omega$  resistor network,  $R_{F1}=2 \text{k}\Omega$  resistor network,  $R_{F2}=1 \text{k}\Omega$  resistor network,  $C_{RES}=30\mu F$  made using 3x parallel connected Panasonic ECQ-E2106KF 10 $\mu F$  film capacitors,  $C_F=470\text{pF}$ , NP0, ceramic capacitor,  $C_{HYS} = 10\text{pF}$ , NP0, ceramic capacitor. The  $R_{F1}$  network needs to be sized for DC power dissipation. The  $R_B$  network can be sized according to its single pulse power curves. The MOSFET driver  $U_5$  needs to be placed close to  $Q_1$ . The interconnecting loop made by  $L_{FLD}$ ,  $C_{RES}$ ,  $Q_1$  should have negligible area. The maximum attainable coil current is limited by power dissipation in  $Q_1$ ; therefore, adequate heatsinking of  $Q_1$  is critical.